

ACTA MATERIALIA TRANSYLVANICA

Material Sciences Publications

Volume 7, Issue 1



ERDÉLYI MÚZEUM-EGYESÜLET
Kolozsvár
2024

A folyóirat megjelenését támogatta a Communitas Alapítvány, a Magyar Tudományos Akadémia, a Bethlen Gábor Alapkezelő Zrt. és az EME Műszaki Tudományok Szakosztálya / The publication of this magazine was supported by the Communitas Foundation, by the Hungarian Academy of Sciences, by the Bethlen Gábor Fund and by the TMS – Department of Engineering Sciences.



Főszerkesztő / Editor-in-Chief: Bitay Enikő

Nemzetközi Tanácsadó testület / International Editorial Advisory Board:

Prof. Biró László Péter, MTA Energiatudományi Kutatóközpont, Budapest, Magyarország
 Prof. emer. B. Nagy János, University of Namur, Namur, Belgium
 Prof. Czigány Tibor, Budapesti Műszaki és Gazdaságtudományi Egyetem, Budapest, Magyarország
 Prof. Diószegi Attila, Jönköping University, Jönköping, Svédország
 Dobránszky János, HUN-REN-BME Kompozittechnológiai Kutatócsoport, Budapest, Magyarország
 Prof. Dusza János, Institute of Materials Research of Slovak Academy of Sciences, Kassa, Szlovákia
 Prof. Kaptay György, Miskolci Egyetem, Miskolc, Magyarország
 Dr. Kolozsváry Zoltán, Plasmaterm Rt., Marosvásárhely, Románia
 Prof. Mertinger Valéria, Miskolci Egyetem, Miskolc, Magyarország
 Prof. Porkoláb Miklós, Massachusetts Institute of Technology, Cambridge, MA, USA
 Prof. Réger Mihály, Óbudai Egyetem, Budapest, Magyarország
 Prof. emer. Réti Tamás, Óbudai Egyetem, Budapest, Magyarország
 Prof. emer. Roósz András, Miskolci Egyetem, Miskolc, Magyarország
 Dr. Spenik Sándor, Ungvári Nemzeti Egyetem, Ungvár, Ukrajna
 Prof. Zsoldos Ibolya, Széchenyi István Egyetem, Győr, Magyarország

Lapszámszerkesztők / Editorial Board:

Dobránszky János, HUN-REN-BME Kompozittechnológiai Kutatócsoport, Budapest, Magyarország
 Csavdári Alexandra, Babeş-Bolyai Tudományegyetem, Kolozsvár, Románia
 Gergely Attila, Sapientia Erdélyi Magyar Tudományegyetem, Marosvásárhely, Románia
 Kovács Tünde, Óbudai Egyetem, Budapest, Magyarország

Kiadó / Publisher: Erdélyi Múzeum-Egyesület

Felelős kiadó / Responsible publisher: Biró Annamária

Olvasószerkesztő / Proofreader: Szenkovics Enikő (magyar), David Speight (English)

Szerkesztőségi titkár / Editorial secretary: Kisfaludi-Bak Zsombor

Borítótér / Cover: Kőnczey Elemér

Nyomdai munkálatok / Printed at: F&F International Kft., Gyergyószentmiklós

Copyright © a szerzők / the authors, EME/ TMS 2024

ISSN 2601-1883, ISSN-L 2601-1883

DOI: 10.33923/amt-2024-02

A folyóirat honlapja: <https://www.eme.ro/publication-hu/acta-mat/mat-main.htm>

The journal website: <https://www.eme.ro/publication/acta-mat/mat-main.htm>

Az *Acta Materialia Transylvanica. Anyagtudományi Közlemények* az Erdélyi Múzeum-Egyesület (EME) Műszaki Tudományok Szakosztályának folyóirata, amely az anyagtudományok területéről közlő tudományos közleményeket: szakcikkeket, összefoglalókat (szemléket), tanulmányokat. A folyóirat célja összképet adni kiemelten a Kárpát-medencei kutatási irányokról, tudományos eredményeiről, s ezt széles körben terjeszteni is. A folyóirat az EME felvállalt céljaihoz híven a magyar szaknyelv ápolását is támogatja, így a nyomtatott folyóirat magyar nyelven jelenik meg, mely az Erdélyi digitális adattárban elérhető (<https://eda.eme.ro/handle/10598/30356>). A széles körű nemzetközi terjesztés érdekében a folyóirat teljes angol nyelvű változatát is közzétesszük.

Acta Materialia Transylvanica – Material Sciences Publications – is a journal of the Technical Sciences Department of the Transylvanian Museum Society, publishing scientific papers, issues, reviews and studies in the field of material sciences. Its mission is to provide and disseminate a comprehensive picture focusing on research trends and scientific results in the Carpathian basin. In accordance with the general mission of the Transylvanian Museum Society it aims to support specialized literature in Hungarian. The printed version of the journal is published in Hungarian and is available in the Transylvanian Digital Database (<https://eda.eme.ro/handle/10598/30356>). However, we would like to spread it internationally, therefore the full content of the journal will also be available in English.

Tartalom / Content

KERÉNYI GÁBOR, RÁCZI VIKTOR GERGELY	59
<i>CNC-marógépen végzett mérés pontosságának meghatározása</i>	
<i>Determining the Accuracy of Measurement on a CNC Milling Machine</i>	
KERTÉSZ OLIVÉR GÁBOR, TÓTH LÁSZLÓ	66
<i>Öntőszerszámok élettartamának növelése mélyhűtéses hőkezeléssel</i>	
<i>Extending the Lifetime of Die Casting Tools with Cryogenic Heat Treatment</i>	
KISS ATTILA, WELTSCH ZOLTÁN	71
<i>A hidrogén-benzin-levegő keverék hatása a belső égésű motorok emissziós értékeire – áttekintés és perspektívák</i>	
<i>Effect of the Hydrogen-Gasoline-Air Mixture on the Emission Values of Internal Combustion Engines. Overview and Perspectives</i>	
KORSÓS KRISZTIÁN, KOVÁCS DORINA	77
<i>A kopási tulajdonságok vizsgálata duplex felületkezelésű 42CrMo4 acélon</i>	
<i>Investigation of Wear Properties on Duplex Surface-treated 42CrMo4 Steel</i>	
KUTI JÁNOS, FÁBIÁN ENIKŐ RÉKA, GÁTI JÓZSEF	82
<i>A vágógázok hatása a termikusan vágott, nagy szilárdságú acélok keménységére</i>	
<i>Effect of Cutting Gases on the Hardness of Thermally Cut High Strength Steels</i>	
MÉSZÁROS BÉLA, FÁBIÁN ENIKŐ RÉKA	88
<i>A felületmegmunkálás hatása a lézeres felületedzés eredményességére</i>	
<i>The Effect of Surface Machining on the Efficiency of Laser Surface Treatment</i>	
NAGY DÁNIEL, KATULA LEVENTE TAMÁS	94
<i>Acél és alumínium vékony lemezek hegesztőforrasztott kötéseinek vizsgálata</i>	
<i>Examination of the Weld Brazed Joints of Steel and Aluminium Thin Plates</i>	
RÁCZI VIKTOR GERGELY, MIKÓ BALÁZS	100
<i>Lézeres gravírozás CNC-marógépen</i>	
<i>Laser Engraving on a CNC Milling Machine</i>	

SCHRAMKÓ MÁRTON, STADLER RÓBERT GÁBOR, PINKE PÉTER, KOVÁCS TÜNDE ANNA109

Polipropilénlemezek ultrahangos hegesztésének optimalizálása

Optimization of Ultrasonic Welding of Polypropylene Sheets

VACZKÓ DÁNIEL, WELTSCH ZOLTÁN, KERESZTES RÓBERT113

*Femtosekundumos lézerrel végzett felületkezelés hatásai pultrúzióval gyártott
üvegszállal erősített kompozitokon*

*Effects of Femtosecond Laser Surface Treatment on Glass Fiber Reinforced Composites
Produced by Pultrusion*



Determining the Accuracy of Measurement on a CNC Milling Machine

Gábor KERÉNYI,¹ Viktor Gergely RÁCZI²

¹ Obuda University, Banki Donat Faculty of Mechanical Engineering, Budapest, Hungary, gaborkerenyi5@gmail.com

² Obuda University, Doctoral School on Safety and Security Sciences, Budapest, Hungary, raczi.viktor@bgk.uni-obuda.hu

Abstract

This article describes the difference between coordinate measurement results obtained on a coordinate measuring machine and on a CNC milling machine. It also includes the raw materials used for measurement, the geometry of the workpiece used, the tools used, the principles used to evaluate the measurement and the measurement results. In terms of measurement results, machine measurement has been shown to be more accurate. For flatness, the deviation between the two measurements averaged 4 μm , for circularity 4 μm , for single-interpolation machining with one axis 3 μm , their parallelism 5 μm , for machining two ten-slots together 2 μm , their parallelism 5 μm . The difference between the errors proves that milling and measuring machine measurement do not differ to such an extent as to require investment in a measuring machine, if circumstances do not require it.

Keywords: metrology, coordinate measurement, CNC milling machine, accuracy.

1. Introduction

An important principle of manufacturing is to achieve dimensional accuracy and precision by means of a tool. These tools can be any of the machines used in manufacturing technology, whether driven by human power, heat, electricity, or any energy source discovered since our existence on earth. One of the most important problems we face has always been and will always be to achieve the necessary precision.

In the world of Industry 4.0 and automation, metrology has also become part of the equation, which has increased the frequency with which measuring machines are integrated into production. Both in-production and post-production measurements are an important way to improve accuracy. Two systems have become widely used in industry: on-machine measurement (OMM) and coordinate machine measurement (CMM).

OMM is a process that allows machine tools to measure and evaluate the dimensions and geometric properties of workpieces immediately after the manufacturing process and is also used for in-process measurements. As a result, the OMM

system allows manufacturers to get real-time feedback on the accuracy of production and to apply corrections immediately if necessary. In this way, OMM can help to increase manufacturing efficiency and improve quality.

The term CMM stands for coordinate measuring machine. A coordinate measuring machine is a device used during and after the manufacturing process to measure and check the dimensions and geometric properties of workpieces. The CMM is a high-precision CNC-controlled system capable of accurately measuring the X, Y and Z coordinates of objects. CMMs allow manufacturers to check workpieces against design specifications and evaluate the accuracy and quality of the production process. However, the cost of such a measuring machine is very different from the tools used in the OMM process mentioned above, and its use is regulated by more stringent and binding standards. It also requires a specialist to operate the measuring machine, which adds to the cost of producing the parts.

Within the framework of Industry 4.0, it is possible to use automated systems. For OMM tools that

are integrated into the system, it is important to assess the degree of reliability and accuracy of the tool and to consider whether the cost reduction is worthwhile. In contrast, in additive manufacturing, OMM is the preferred application where a hybrid machine is available that can perform both additive manufacturing and machining. In such cases, it is not practical to take the part out of the machine, so OMM should be used, further reducing the number of defects introduced.

The aim of this study is to compare the accuracy of OMM and CMM measurements.

In manufacturing and its inspection, there has always been the question of whether an expensive but accurate coordinate measuring machine is needed, or whether we should settle for the now common and relatively cheap probing units that can be installed in the machine tool. When OMM systems are used, the vast majority of companies use touch probes only for zero-point measurement, and a small percentage try to integrate them into production to a level where they can determine the size compensation value after machining. This gives them an accurate value more quickly to make the correction than after the operators have measured. The paper also discusses how the problem is to be investigated and what tools are to be used to carry out the exercise.

The following chapters will further elaborate on the specifications of the materials used and the measurement methods and guidelines used.

2. Measurement evaluation methods

The evaluation method also differed between the two machines used in the measurement. For the Renishaw gauge head used in the CNC machine, we did not use the evaluation methods offered by the manufacturer and therefore used the Excel program for the OMM. The evaluation of the measurement on the coordinate measuring machine was carried out using the Mitutoyo program (Geopak v2.3 R10). In both cases the same points were measured, and the results were calculated using the same method.

There are several methods for evaluating the points obtained during the measurement. We used the method of fitting, the Gaussian least squares method, which is also used in industry. To apply this method, we had to use the following basic equations for the different geometric elements:

$$\text{Plane: } Ax + By + C = 0 \quad (1)$$

$$\text{Linear: } Ax + By + Cz + D = 0 \quad (2)$$

$$\text{Circle: } Ax^2 + Ay^2 + Cx + Dy + E = 0 \quad (3)$$

where A, B, C, D, E are the normal vector components and x, y, z are the coordinates of the given point (1), (2), (3) [1].

2.1. The gaussian curve fitting

In nature (because of the central limiting distribution theorem), measurable quantities usually have a Gaussian distribution, i.e., if the expected / theoretical value of a measurable quantity is μ , then the distribution of measured values will follow a Gaussian curve around μ , the width of which is proportional to the error of the measurement.

However, if we are not testing a single measurement in a sequentially repeatable manner, but pairs of data, that is a quantity according to a given function, then we use a modified χ^2 test (4).

$$\chi^2 = \sum_{i=1}^N \left(\frac{f_i - f(x_i)}{\Delta f_i} \right)^2 \quad (4)$$

The theoretical function that we take as a basis is $f(x_i)$ and x_i is the value of the function at that point. The formula can be used to examine the probability that, given the given theoretical function, the measurement points obtained in practice will be obtained. The value of χ^2 gives the probability and has two parameters. One is the theoretical function itself and the other is the number of measurement points, that is, the number of degrees of freedom. If the value of the probability is less than 0.1 % then the theory is not correct and can be rejected, but otherwise it undermines the hypothesis.

The Gaussian fit we use is the inverse of this relationship. In the case where we are looking for a function by varying the parameters, we are looking for the minimum value of χ^2 (minimizing it), so we obtain the optimal parameters. This is called fitting [2].

2.2. The gaussian linear fitting

For the Gaussian fit of OMM, we used the Excel Solver numerical algorithm. Where the points were located along each line, a line was fitted to the measured points using Excel. In this case the relation of the quantity to be minimized is (5):

$$\chi^2(a, b) = \sum_{i=1}^N \left(\frac{f_i - ax_i - b}{\Delta f_i} \right)^2 \quad (5)$$

To check the minimalisation, we also calculated the optimal parameters using other methods. Using the equation of the line by a non-numerical method. Equation of the line is (6):

$$Y = ax + b \quad (6)$$

where a slope, b the point where the line intersects the Y-axis. To determine the slope, perform the following operation. Here, the coordinates x and y of the measured points and their mean (\bar{x}) are calculated (7).

$$a = \frac{\sum(x - \bar{x})(y - \bar{y})}{\sum(x - \bar{x})^2} \quad (7)$$

The value b is solved by the following equation. The idea is that the line must pass through the points \bar{x} and \bar{y} , so we will substitute this into the equation of the line. Then we sort the equation and get the intercept of the y-axis (8).

$$\bar{y} = a\bar{x} + b \rightarrow b = \bar{y} - a\bar{x} \quad (8)$$

Both methods gave the same result when written out to 4 decimal places, so the evaluation method can be considered correct.

The straightness of the geometric element under consideration was defined as the difference between the maximum and minimum of the measured points.

2.3. The gaussian circle fitting

We also used minimization for the circle but changed other parameters and approximated to obtain the optimal values.

For the calculation we used 24 measurement points defined by x and y coordinates.

The Pythagorean theorem was used to calculate the value of R_i (radius associated with x and y) as a function of the measurement points (9). The centre of the circle is indexed x_0 and y_0 in the calculation and has a default value of 0.

$$R_i = \sqrt{(x_i - x_0)^2 + (y_i - y_0)^2} \quad (9)$$

We also needed the value of ΔR which is the difference between the nominal value of R and R_i (10).

$$\Delta R = R - R_i \quad (10)$$

It was also necessary to sumsquare the ΔR .

In the minimization, x_0 , y_0 and R were varied as a function of $\sum \Delta R$. The circularity was given by the difference between the maximum and minimum of ΔR_i .

3. The applied tools

3.1. The NASA-test

The accuracy of machining is greatly influenced by the elements of the workpiece-machine-device-tool (WMDT) system. The US National Aeronautics and Space Administration (NASA) has

developed a test piece to determine the accuracy of this system. The test piece contains surfaces and dimensions that can be used to measure the accuracy of the machine during machining. The test piece is based on a square with a circle on the base and a square rotated 45° on the circle. The test piece is shown in **Figure 1**.

The square machining of the first level from the bottom allows the longitudinal and transverse rake of the table to be measured. With the circle above it, the errors of circular interpolation can be measured, and the errors of axes flattening, and direction change due to circularity errors can be evaluated. The rotated square at the top of the piece gives the errors of the straight-line interpolation. The terraces define the positioning accuracy along the Z axis [3, 4].

The workpiece material was Necuron 651 (artificial wood), which is a polyurethane foam. This material was chosen because it requires little cutting force to machine it, so errors due to cutting parameters are negligible. It also has a better coefficient of thermal expansion than steel, which was necessary because the two machines under test were not located in an air-conditioned room and were also in a different room.

Main features of Necuron 651:

- Cutting force ($kc_{1,1} = 120 \text{ N/mm}^2$);
- Easy chip handling;
- Compressive strength (25 N/mm^2);
- Coefficient of thermal expansion ($40 \cdot 10^{-6} \text{ K}^{-1}$).

3.2. Renishaw probing unit

Both the OMM (Renishaw OMP40-2) and CMM (Renishaw MH20i) probing units used in the measurement are of the switch type. They are the most widely used in the industry due to their commodity and simple principle of operation, which is why they were chosen to perform the

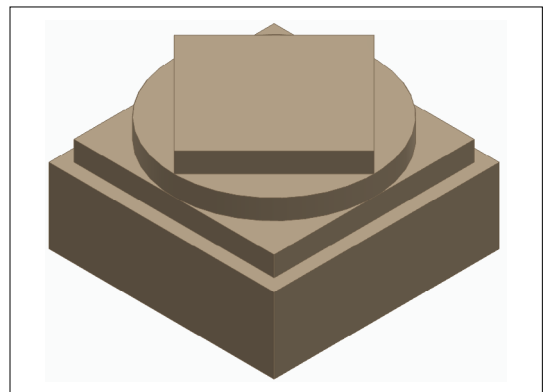


Fig. 1. NASA test (workpiece).

measurements. The manufacturer uses the term kinematic probe. They are measuring devices based on resistance variation and operate on the following principle.

In the probe head shown in **Figure 2**, three equally spaced rods rest on six hardened carbide balls, providing six contact points in the circuit. An electrical circuit is created through these connection points **Figure 2 (a)**. The structure is preloaded by a spring, so the circuit is closed. Due to the spring load, interfaces are created through which the voltage flows **Figure 2 (b)**. At the moment of probing, the reaction force in the opposite direction to the working force in the probing structure leads to a reduction of the interface **Figure 2(c)**, resulting in an increase in resistance at that point **Figure 2 (d)**. The variable force on the interface is measured as the change in the circuit. When the change in resistance reaches a limit, the output of the probe signals and sends a „tap” signal to the PLC-controller [5, 6].

In the case of the OMM, the touch probe communicates with the controller by optical signal transmission, whereas the coordinate measuring machine is directly connected to the controller.

The probe is made of industrial ruby.

3.3. The HAAS CNC milling machine

For the OMM measurement, a Haas Mini Mill Edu type 3-axis machining centre was used. The machine tool is a milling machine designed for educational purposes. Machine choice was based on the fact that the machine is equipped with a measuring system capable of optical signal transmission for OMM measurement, and the milling machine is a newly manufactured model, so possible wear errors can be neglected. The main spindle can be indexed in only one position. The machine is shown in **Figure 3** [7].

The probing unit we use is the Renishaw OMP40-2, which has a repeatability of 1 μm . The length of the probe is 50 mm [8].

3.4. Coordinate measuring machine

The coordinate measuring machine was selected according to our capabilities. A Mitutoyo Crysta Plus M574 was chosen (**Figure 4**).

The measuring machine is equipped with an air bearing on all axes and a measuring gauge to ensure accuracy. The working space is 500×700×400 mm. The accuracy of the measuring machine is $E = 3.5 + 4.5L/100 \mu\text{m}$, and the resolution is 0.5 μm [9].

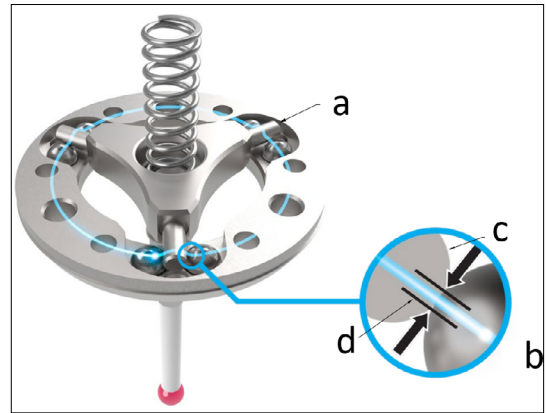


Fig. 2. Switch type probe operating principle. [5]



Fig. 3. Haas Mini Mill Edu milling machine centre.



Fig. 4. Mitutoyo Crysta Plus M574 measuring machine.

In the coordinate measuring machine Renishaw MH20i type probe unit was used. The size of the ruby sphere was 3 mm. The repeatability of the probe is 1.5 μm [10].

3.5. Control of probing units

In the case of the coordinate measuring machine, the program was created by teaching the points to be touched. For both OMM and CMM measurements, we used the same strategy and alignment length to ensure that any positioning inaccuracies or machine errors would affect the measurement under the same conditions (e.g., misalignment, etc.). During the measurements, the workpiece zero-point was centred in the upper plane of the workpiece.

For the CNC machine, we used G-code programming to create the point cloud. The G-codes that we used were called from Renishaw’s own sub-routines using G65, a simple macro call [11].

Renishaw subprogram:

- P9832 – Probe unit start;
- P9810 – Protected movement;
- P9811 – Simple surface measurement;
- P9821 – Simple surface angle measurement.

4. Results

During the measurement, several measurements were taken, and the average of these measurements is summarised in the tables.

4.1. OMM and CMM measurement results

To evaluate the OMM measurements, we used an Excel extension, Solver. The correctness of the obtained values (uniformity, parallelism) was also checked by elementary calculations.

Flatness was measured in the upper plane of the workpiece, the value of which is entered in **Table 1**. The number of measuring points was 9 in both cases (**Table 1**).

Figure 5 shows the measurement points of the square island rotated by 45° and the regression line fitted to the points and describes the equation of the lines. From the measurement it can be seen that the CNC machine axes are not yet worn out to a level that can be detected by such a measurement. The axes move together with high precision. This can be seen from the slope of the regression lines. The difference in slope is only 0.0001 for the E3 line. For the other lines the deviation is smaller. In the equation of the line, the constant value differs from the nominal value (40 mm), the reason being that the milling tool used for the machining was not accurately dimen-

Table 1. Upper plane measurement results

Parameter	OMM value (mm)	CMM value (mm)
Flatness	0.0033	0.0070
Max	-0.0159	0.0050
Min	-0.0192	-0.0020

Table 2. The square shape rotated by 45° measurement results

Linearity and parallelism		
Line	OMM value (mm)	CMM value (mm)
E1 (-X; -Y)	0.0028	0.0060
E2 (X; Y)	0.0030	0.0043
E3 (-X; Y)	0.0038	0.0038
E4 (X; -Y)	0.0027	0.0035
E1×E2	0.0031	0.0113
E3×E4	0.0034	0.0069

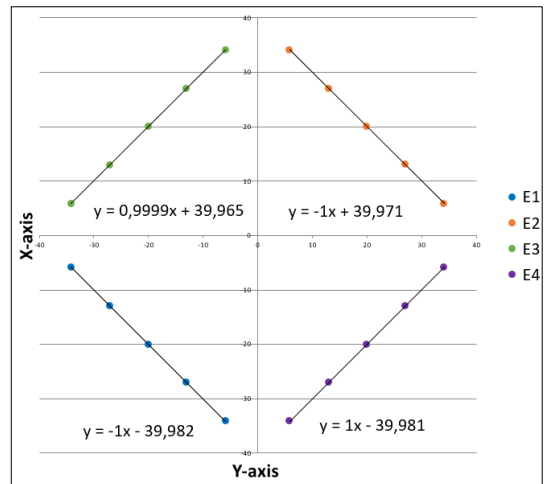


Fig. 5. OMM measurement result of a square rotated by 45°.

sioned, so the diameter of the milling tool differed from the value given in the correction table [12].

Table 2 compares the OMM and CMM measurement results.

The circular island was measured with 24 points 15° apart. A Gaussian fitting method was applied to the measurement results. The probed diameter was 80 (mm). **Figure 6** shows the point cloud used for the circular shape measurement.

The parameters of the measured circle were defined, where x_0, y_0 are the coordinates of the

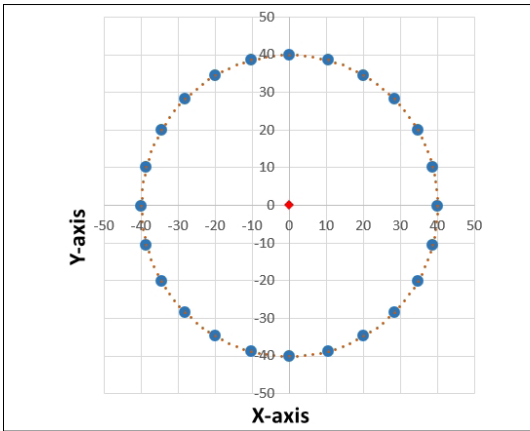


Fig. 6. OMM measurement of the round shape with 24 points.

Table 3. Round shape measurement results

Circle parameters	OMM value (mm)	CMM value (mm)
x_0	-0.0014	0.0020
y_0	-0.0035	0.0040
R	39.9772	39.9860
D	79.9544	79.9720
Min	0.0020	-0.0050
Max	-0.0047	0.0050
RND	0.0067	0.0110

Table 4. The square shape measurement results

Linearity and parallelism		
Line	OMM value (mm)	CMM value (mm)
E1 (X+)	0.0030	0.0069
E2 (X-)	0.0036	0.0068
E3 (Y+)	0.0050	0.0066
E4 (Y-)	0.0047	0.0073
E1×E2	0.0067	0.0207
E3×E4	0.0058	0.0103

Table 5. The circular shape upper plane measurement results

Circular shape upper plane		
Parameters	OMM value (mm)	CMM value (mm)
Flatness	0.0047	0.0070
Max	-8.0034	-8.0040
Min	-7.9986	-7.9970

centre of the circle, R is the radius of the circle, D is the diameter of the circle, Min is the minimum deviation from the Gaussian circle and Max is the maximum deviation, and RND is the circularity error (Table 3).

When milling a square shape, the axes moved independently of each other so that displacement occurred along only one axis (Table 4).

The surface of the circle shape was also checked for flatness. We recorded 3 points per quadrant on the surface, giving 12 measurement points. A plane was fitted to the measured points and the evaluation is shown in the following table (Table 5).

We also measured flatness at the lowest Z level out of 4 points. In this case, the plane fitted to the points was also evaluated (Table 6).

5. Conclusion

When comparing the data, the coordinate measurement on the measuring machine always more differs from the nominal value (max. 0.004 mm) than the results measured on the CNC machine (max. 0.003 mm), which depends on the accuracy of the measurement. The CMM measurement has a higher resolution due to the size of the ruby ball (Chapter 3.3 and Chapter 3.4), as it is smaller and therefore more sensitive to deviations, and therefore the deviation will be larger. In the case of the CNC, the deviation may also be caused by the difference in resolution due to the rotary encoder of the machine, as the measuring machine is equipped with a measuring gauge, therefore the higher resolution also leads to the higher sensitivity.

The same trend is observed for the flatness and its maximum and minimum values, with CMM measurements having a larger error (7 μm) than OMM measurements (4 μm).

The measurement results are relevant for industrial applications as the cost of coordinate measurements varies according to the equipment used. The CNC machine used and the Renishaw

Table 6. The square shape upper plane measurement results

Square shape plane		
Parameters	OMM value (mm)	CMM value (mm)
Flatness	0.0037	0.0000
Max	-16.0055	-16.0000
Min	-16.0018	-16.0000

OMP40-2 measuring device mounted on it allow measurements to be made more economically with sufficient accuracy.

References

- [1] Hocken R. J., Pereira P. H. (eds.): *Coordinate Measuring Machines and Systems*. Manufacturing Engineering and Materials Processing, CRC Press, New York, 2011.
<https://doi.org/10.1201/b11022>
- [2] Csanád Máté: Környezetfizikai Laboratóriumi Gyakorlatok. Méréskiértékelés (accessed: 2023. 04. 30.)
<https://atomfizika.elte.hu/kornyfizlab/docs/mesreskiertekeles.pdf>
- [3] Hervay P.: *Szerszámgép sajátpontosságának vizsgálata II*. NSZFI. (accessed on: 2023. április 30.)
https://www.nive.hu/Downloads/Szakkepzesi_dokumentumok/Bemeneti_kompetenciak_meresi_ertekelesi_eszkozrendszerenek_kialakitasa/5_0275_010_101215.pdf
- [4] Barnfather J. D., Goodfellow M. J., Abram T.: *Photogrammetric measurement process capability for metrology assisted robotic machining*. Measurement, 78. (2016) 29–41.
<https://doi.org/10.1016/j.measurement.2015.09.045>
- [5] Renishaw.com: Probing systems for CNC machine tools. (letöltve: 2023. április 30.)
<https://www.renishaw.com/resourcecentre/download?data=117597&lang=en&userLanguage=en>
- [6] Marcelo Del Guerra, Reginaldo Teixeira Coelho: *Development of a low cost Touch Trigger Probe for CNC Lathes*. Journal of Materials Processing Technology, 179/1–3. (2006) 117–123.
<https://doi.org/10.1016/j.jmatprotec.2006.03.093>
- [7] Haas Automation gyártó cég weboldala: Haas Mini Mill EDU (accessed on: 2023. 05. 21.)
<https://www.haascnc.com/hu/machines/vertical-mills/mini-mills/models/minimill-edu.html>
- [8] Renishaw OMP40-2 műszaki dokumentáció (letöltve: 2024. május 21.)
<https://www.renishaw.com/resourcecentre/en/details/Data-sheet-OMP40-2--131542?lang=en>
- [9] Mitutoyo Mitutoyo Crysta-plus M574 típusú mérőgép adatlap. (accessed on: 2024. május 7.)
[https://shop.mitutoyo.hu/web/mitutoyo/hu_HU/mitutoyo/CRYSTA-APEX%20S900%20Series/CRYSTA-Apex%20V544%20CNC%20CMM/\\$catalogue/mitutoyoData/PR/191-121/index.xhtml](https://shop.mitutoyo.hu/web/mitutoyo/hu_HU/mitutoyo/CRYSTA-APEX%20S900%20Series/CRYSTA-Apex%20V544%20CNC%20CMM/$catalogue/mitutoyoData/PR/191-121/index.xhtml)
- [10] Renishaw MH20i műszaki dokumentáció (letöltve: 2024. május 21.)
<https://www.renishaw.com/resourcecentre/en/details/Data-sheet-MH20-and-MH20i--18222?lang=en>
- [11] Renishaw programozási útmutató (accessed on: 2024. 05. 21.)
<https://www.haascnc.com/content/dam/haascnc/en/service/reference/probe/renishaw-inspection-plus-programming-manual--2008.pdf>
- [12] Choi J. P., Min B. K., Lee S. J.: *Reduction of machining errors of a three-axis machine tool by on-machine measurement and error compensation system*. Journal of Materials Processing Technology, 155–156. (2004) 2056–2064.
<https://doi.org/10.1016/j.jmatprotec.2004.04.402>



Extending the Lifetime of Die Casting Tools with Cryogenic Heat Treatment

Kertész Olivér Gábor,¹ Tóth László²

¹ Bánki Donát, Faculty of Mechanical and Safety Engineering, Óbuda University, Budapest, Hungary, k.oliver0917@gmail.com

² Bánki Donát, Faculty of Mechanical and Safety Engineering, Óbuda University, Budapest, Hungary, toth.laszlo@bgk.uni-obuda.hu

Abstract

In our work, we aimed to increase the lifespan of tools used in pressure die casting. We conducted experiments on test specimens made from two types of base materials, which were subjected to various heat treatments, followed by material testing on the specimens. In parallel, the final tools were also produced, and parts were manufactured using these tools. Based on the results of the experiments and production, considering both quality and economic aspects, the most suitable base material proved to be the electroslag remelted tool steel, for which we applied cryogenic heat treatment. To enhance the tool lifespan, we performed additional heat treatments on the optimal material, as well as optical microscopy examinations and hardness measurements.

Keywords: *tool steel, die, lifetime, cryogenic treatment.*

1. Introduction

Pressure die casting is used for the production of precise castings with complex geometries, primarily for automotive parts. To achieve the required cleanliness, homogeneity, and optimal microstructure of the product, it is essential to carefully select the raw materials and design an appropriate manufacturing process [1, 2]. The quality of the die-casting tool material also depends on the steel manufacturing process, which can include conventionally produced, remelted, or powder metallurgy-produced materials [3]. In our experiments, we conducted tests on two material grades: a conventionally cast and an electroslag remelted material. Electroslag remelted steel differs from conventionally produced steel in that it is cleaner, free from contaminants, almost inclusion-free, and structurally more homogeneous. Other characteristics of electroslag remelting include the absence of macro-segregation, minimal micro-segregation, and excellent material properties [4].

The selected materials belong to the family of hot-work tool steels, which are characterized by three primary properties: hot strength, hot toughness, and hot wear resistance. These properties can be achieved through their chemical composition and appropriate heat treatment. The conventional heat treatment process for hot-work tool steels consists of stress relief, hardening, and tempering. An alternative process is cryogenic heat treatment, which was applied along with conventional heat treatment in our study. Among these, cryogenic heat treatment proved to be the most effective, as evidenced by the achieved hardness values and the favorable microstructure. In the microstructure following cryogenic treatment, the amount of retained austenite is minimal.

The lifespan of die-casting tools is characterized by the so-called shot count, which indicates the number of shots the tool can withstand under optimal operating conditions without intervention. According to the literature, this number ranges between 75,000 and 150,000 shots for aluminum castings [1, 2].

2. Materials, Equipment, Devices, Methods

2.1. Material Selection

In our study, we experimented with a pressure die-casting tool for an aluminum car seal housing. This tool has a complex shape with varying wall thicknesses, making it sensitive to heat, pressure, and different types of stresses. When selecting the tool material, we need to consider properties that affect its lifespan. The objective is to minimize wear processes and prevent cracking and tool breakage. For hot-work tool steels, resistance to thermal fatigue – essential to preventing crack formation – is a key factor in addition to handling various stresses [5].

The most important alloying element in tool steels is carbon, which significantly impacts the properties of the alloy. Increasing carbon content enhances strength and hardenability but decreases ductility, formability, weldability, and machinability. Silicon primarily acts as a deoxidizer and also increases strength, wear resistance, and heat resistance. Manganese acts as a deoxidizer and, by forming manganese sulfide with sulfur, prevents red brittleness, reduces the critical cooling rate, and improves hardenability. Chromium is a carbide-forming alloying element that, like manganese, lowers the critical cooling rate, thereby enhancing hardenability and through-hardening capability, as well as improving hot strength and scale resistance. Molybdenum, another carbide-forming alloying element, also serves to reduce the critical cooling rate, thus improving hardenability and through-hardening capability. It promotes fine grain formation and increases strength and wear resistance. Vanadium is a very strong carbide former that enhances toughness, hot strength, and temper resistance [6].

Initially, we used Böhler W302-grade tool steel, a hot-work tool steel produced by conventional casting. A tool made from this material, when conventionally heat-treated, was able to perform 6,000 defect-free shots during operation. At that point, micro-cracks appeared in the critical cross-section of the tool, which were repaired by overlay welding, but this only marginally extended its lifespan [7]. We then experimented with Uddeholm Unimax, an electroslag remelted tool steel. The chemical compositions of these steels are shown in Table 1.

Table 1. Chemical Composition of the Tool Steels Used

	C (%)	Si (%)	Mn (%)	Cr (%)	Mo (%)	V (%)
W302	0.39	1.0	0.40	5.20	1.40	0.95
UNIMAX	0.50	0.20	0.50	5.00	2.30	0.50

2.2. Tools and Equipment

2.2.1. The Heat Treatment Furnace

The tools were heat-treated in a Schmetz-type vacuum furnace (Figure 1). The electric vacuum furnace operates by heating in a vacuum, cooling with nitrogen gas, and cryogenically cooling through the spraying and injection of liquid nitrogen.

2.2.2. Microscopic Microstructure Examination

The optical microscopic microstructure examination was conducted using a Neophot 2 light microscope, and the images were taken at a magnification of 1000×.

2.2.3. Heat Treatment of Böhler W302 Tool Steel

The heat treatment is generally followed by a final sizing process, which is why the planning of the heat treatment technology is very important, as it determines the tool's final properties. The heat treatments consist of heating, holding at temperature, and cooling. In the case of a pressure die-casting tool, stress relief, hardening, and tempering are applied.



Fig. 1. The Heat Treatment Furnace.

2.2.3.1. Stress Relief Annealing

Stress relief is necessary to eliminate the residual stresses formed during the manufacturing of the tool. Thermal internal stresses can also form after hardening, which may combine with the residual stresses created during manufacturing. The total of these stresses can lead to micro-cracks and fractures. Therefore, stress relief before manufacturing and heat treatment is crucial. During the stress relief process, the tool was slowly heated to 650 °C in a 2 bar nitrogen protective gas environment, held at that temperature for 2 hours, and then slowly cooled to room temperature (**Figure 2**).

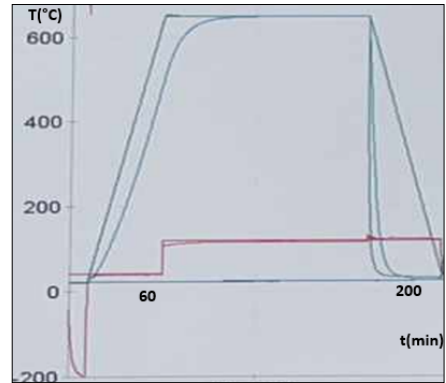


Fig. 2. Stress Relief Annealing

2.2.3.2. Hardening

Stress relief was followed by hardening, during which a three-step heating process was used in a vacuum to equalize the temperature between the surface and the core before structural transformations, with the goal of preventing stresses caused by phase changes. The hardening temperature for the tool made from Böhler W302 material was set at 1020 °C. After reaching this temperature, a 15-minute holding period followed to allow the formation of homogeneous austenite (**Figure 3**).

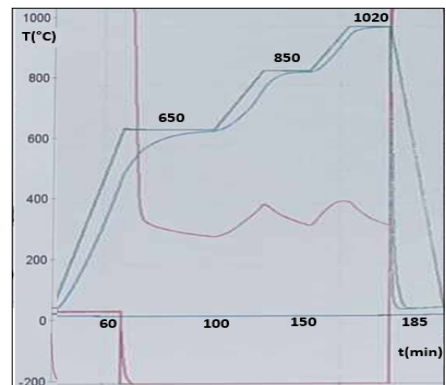


Fig. 3. Hardening

2.2.3.3. Tempering

The purpose of tempering is to adjust the hardness-toughness ratio, reduce stresses, and decrease the amount of retained austenite. For the tool made from Böhler W302 material, we applied three high-temperature tempering cycles (**Figure 4**) [8, 9, 10].

2.3. Heat Treatment of Uddeholm UNIMAX Tool Steel

The purpose of cryogenic heat treatment is to reduce the amount of retained austenite, which leads to improved homogeneity, structural stability, increased hardness, and toughness. By improving these factors, the tool's lifespan is also extended. There are several possible methods for cryogenic treatment, and we used the evaporation and injection of liquid nitrogen. The key principle is that the cooling of the furnace chamber is achieved by spraying and injecting nitrogen, allowing the tool to be cooled to -150 °C. For Uddeholm UNIMAX tool steel, the hardening temperature was set at 1050 °C, and the tool was held at this temperature for 20 minutes [8, 11]. After the holding period, the tool was cooled to 50 °C with 8 bar nitrogen gas, followed by cryogenic

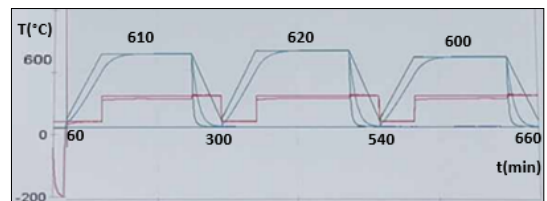


Fig. 4. Tempering

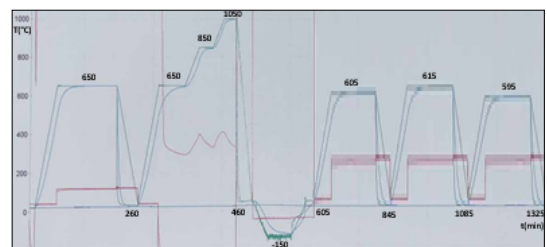


Fig. 5. Heat Treatment Diagram of the Uddeholm UNIMAX Tool Steel.

treatment using liquid nitrogen. The high-temperature tempering cycles were performed in 2 bar nitrogen gas (Figure 5).

3. Measurement Results

3.1. Hardness Measurement

The hardness of the tool made from Böhler W302 after heat treatment is 45 HRC, while the tool made from Uddeholm UNIMAX steel has a hardness of 48 HRC after heat treatment. These results are shown in Table 2.

Table 2. Hardness Values in Tabular Form

Tool Material	Average hardness (HRC)
Böhler W302	45
Uddeholm UNIMAX	48

3.2. Microscopic Microstructure Examination

The microstructure examination was performed after specimen preparation using an optical microscope, as illustrated in Figures 6. and 7. The microscopic images show that in the case of the re-melted and cryogenically treated steel quality, the amount of retained austenite was minimized, and the quantity of secondary carbides increased.

4. Conclusion

The lifespan of pressure die-casting tools can be increased by selecting the appropriate raw material made with the correct manufacturing technology, such as electroslag remelted steel.

The cryogenic treatment applied during the tool's heat treatment reduces the amount of retained austenite and achieves the optimal microstructure, which also leads to an increase in tool lifespan. The lifespan of the car sealing housing die-casting tool in question, with the well-chosen raw material and proper heat treatments, demonstrates excellent results in terms of cost-effectiveness. Thus, the tool's lifespan was successfully increased by nearly 47 times (Table 3.).

Table 3. Lifespans in Tabular Form

Tool Material	Lifespan (number of shots)
Böhler W302	6000
Average	75 000–150 000
Uddeholm UNIMAX	280 000

A further opportunity for increased durability is seen in surface treatment. By applying a suitable PVD coating, the surface hardness and wear resistance can be further increased, thus increasing the tool life. [12, 13].

Acknowledgements

We would like to express our gratitude to the Óbuda University, Donát Banki Faculty of Mechanical and Safety Engineering for providing the laboratory facilities and supporting the university, which made this entire paper possible. We also wish to thank the Transylvanian Museum Society, which provided the opportunity to present the topic and contribute to the realization of the paper at the XXIX. Conference of Young Engineers and Scientists.

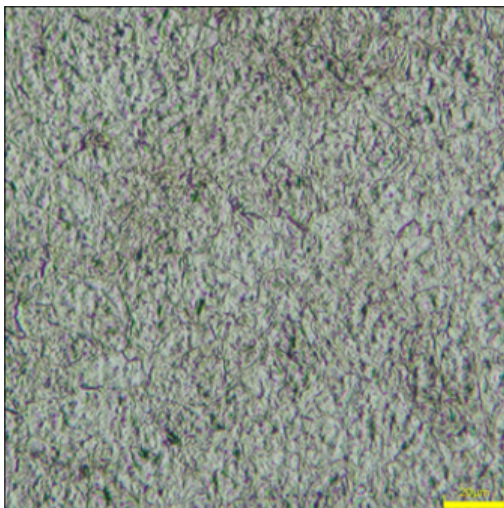


Fig. 6. Microstructure of Böhler W302 Tool Steel, Traditionally Heat Treated

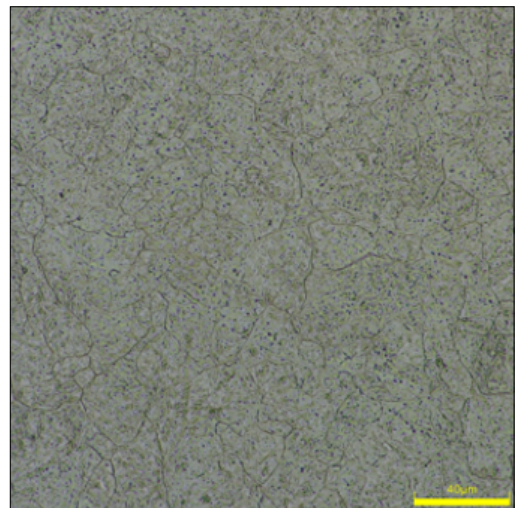


Fig. 7. Microstructure of Uddeholm UNIMAX Tool Steel with Cryogenic Heat Treatment.

References

- [1] Dúl J.: *Nyomásos öntészeti ismeretek* (digitális tananyag). Miskolci Egyetem, 2009.
- [2] Szabó R.: *Öntéstechnikai és hőtechnikai paraméterek hatása az alumínium nyomásos öntvény szilárdsági tulajdonságaira*. (Phd-értekezés) Miskolc, 2012.
- [3] Pribulova A., Futas P., Barosová M.: *Cleanness and Mechanical Properties of Steel after Remelting under Different Slags by ESR*. Key Engineering Materials, 655. (2014) 112–117.
<https://doi.org/10.4028/www.scientific.net/KEM.635.112>
- [4] Halfa H. A., Reda A. M.: *Electroslag Remelting of High Technological Steels*. Journal of Minerals and Materials Characterization and Engineering, 3. (2015) 444–457.
<https://doi.org/10.4236/jmmce.2015.36047>
- [5] Uddeholm AB: Brochure Uddeholm UNIMAX. 2015.
- [6] Hawryluk M., Lachowicz M., Zwierzchowski M., Janik Marta, Gronostajski Z., Filipiak J.: *Influence of the grade of hot work tool steels and its microstructural features on the durability of punches used in the closed die precision forging of valve forgings made of nickel-chrome steel*. Wear, 528–529. (2023) 204963.
<https://doi.org/10.1016/j.wear.2023.204963>
- [7] Böhler Edelstahl GMBH: Brochure W302 Hot Work Tool Steel. 2006.
- [8] Tóth L.: *Reduction of retained austenite in tool steels*. Műszaki Tudományos Közlemények, 16. (2022) 52–57.
<https://doi.org/10.33894/mtk-2022.16.10>
- [9] Artinger I.: *Szerszámacélok és hőkezelésük*. Műszaki Könyvkiadó, Budapest, 1978.
- [10] Szombatfalvy Á.: *A hőkezelés technológiája*. Műszaki Könyvkiadó, Budapest, 1985.
- [11] Mohan L. D., Renganarayanan S., Kalanidhi A.: *Cryogenic treatment to augment wear resistance of tool and die steels*. Cryogenics 41/3. (2000) 149–155.
[https://doi.org/10.1016/S0011-2275\(01\)00065-0](https://doi.org/10.1016/S0011-2275(01)00065-0)
- [12] Dobrzański L. A., Polok M., Adamiak M.: *Structure and properties of wear resistance PVD coatings deposited onto X37CrMoV5-1 type hot work steel*. Journal of Materials Processing Technology, 164–165. (2005) 843–849.
<https://doi.org/10.1016/j.jmatprotec.2005.02.164>
- [13] Bitay E., Tóth L., Kovács T. A., Nyikes Z., Gergely A. L.: *Experimental Study on the Influence of TiN/AlTiN PVD Layer on the Surface Characteristics of Hot Work Tool Steel*. Open Journal of Applied Sciences 11/19 (2021).
<https://doi.org/10.3390/app11199309>
- [14] Schwam D., Wallace J. F.: *Improving Tool Life for Aluminium Die Casting Dies*. 1995.
- [15] Arh B., Podgornik B., Burja J.: *Electroslag Remelting: A Process Overview*. 2016.



Effect of the Hydrogen-Gasoline-Air Mixture on the Emission Values of Internal Combustion Engines. Overview and Perspectives

Attila KISS,¹ Zoltán WELTSCH²

¹ John von Neumann University, Department of Innovative Vehicles and Materials. Kecskemét, Hungary, kiss.attila@nje.hu

² Széchenyi István University, Department of Materials Science and Engineering; Vehicle Industry Research Center. Győr, Hungary, weltsch.zoltan@sze.hu

Abstract

The urgency to combat climate change and reduce dependence on fossil fuels has spurred intense interest in alternative fuels and advanced propulsion technologies. Among these innovations, hydrogen-gasoline dual fuel mode stands out as a transformative approach with the potential to revolutionize internal combustion engines (ICEs) and paves the way for sustainable mobility. This paper provides a comprehensive analysis of the multifaceted implications of hydrogen-gasoline dual fuel combustion, encompassing engine performance optimization, emissions reduction strategies, combustion dynamics elucidation, technological hurdles to overcome, potential applications across diverse sectors, market perspectives, and future research directions.

Keywords: *hydrogen, dual fuel, internal combustion engine.*

1. Introduction

In an era defined by the imperative to address climate change and promote sustainable development, the intersection of mobility and environmental stewardship has become increasingly critical. Against this backdrop, hydrogen emerges as a versatile and promising alternative fuel, offering unparalleled potential to decarbonize transportation and usher in a new era of sustainable mobility. Hydrogen-gasoline dual fuel mode represents a pivotal convergence of tradition and innovation, leveraging the strengths of both hydrogen and gasoline to maximize engine efficiency, minimize emissions, and propel the transition towards a low-carbon future.

2. Hydrogen-Gasoline Dual Fuel Combustion: Maximizing Efficiency and Performance

Hydrogen-gasoline dual fuel combustion represents a groundbreaking approach to optimizing engine efficiency and performance, leveraging the unique properties of both hydrogen and gasoline to achieve unprecedented levels of com-

bustion efficiency and power output. At its core, dual fuel combustion involves the simultaneous combustion of hydrogen and gasoline within the engine's combustion chamber, creating a synergistic blend of fuels that enhances combustion characteristics and unlocks new realms of efficiency [1–4].

2.1. Combustion Enhancement

Hydrogen, with its low ignition energy and wide flammability limits, acts as a combustion enhancer when introduced into the gasoline-air mixture. The addition of hydrogen accelerates the combustion process, promoting more rapid flame propagation and shorter combustion durations. This catalytic effect enhances overall combustion efficiency, leading to improved thermal efficiency and reduced fuel consumption [5, 6].

2.2. Lean-Burn Operation

One of the key advantages of hydrogen-gasoline dual fuel combustion is its ability to enable lean-burn operation, where the air-fuel mixture contains a higher proportion of air relative to fuel. Hydrogen's high-octane rating and fast combus-

tion kinetics allow for stable combustion at leaner air-fuel ratios, reducing fuel consumption and emissions while maintaining engine performance. This lean-burn capability enhances engine efficiency and extends the operational range of the vehicle [7, 8].

2.3. Compression Ratio Optimization

The addition of hydrogen to the combustion process enables higher compression ratios without the risk of engine knock. Hydrogen's resistance to auto-ignition allows for more aggressive compression ratios, leading to improved thermal efficiency and power output. By optimizing compression ratios based on the dual fuel combustion characteristics, engineers can maximize engine efficiency and performance across a range of operating conditions [9, 10].

2.4. Combustion Stability and Flame Propagation

Hydrogen's unique combustion properties, including its high flame speed and low ignition energy, contribute to enhanced combustion stability and flame propagation characteristics. The presence of hydrogen in the combustion chamber accelerates flame propagation, ensuring more uniform and rapid combustion across the entire combustion cycle. This improved combustion stability leads to smoother engine operation, reduced vibration, and enhanced drivability [4, 9].

2.5. Waste Heat Utilization

In addition to optimizing combustion efficiency, hydrogen-gasoline dual fuel combustion offers opportunities for waste heat utilization. The high exhaust temperatures associated with dual fuel combustion can be harnessed for various thermal management applications, such as exhaust gas recirculation (EGR), turbocharging, or waste heat recovery systems. By efficiently capturing and utilizing waste heat, engineers can further improve engine efficiency and overall vehicle performance [4, 9].

2.6. Thermal Efficiency Improvement

Maximizing thermal efficiency is paramount in achieving optimal engine performance and fuel economy. Hydrogen-gasoline dual fuel combustion offers several pathways for enhancing thermal efficiency, including lean-burn operation, higher compression ratios, and waste heat recovery. By operating at lean air-fuel ratios enabled by hydrogen's high-octane rating, engineers can minimize fuel consumption while maintaining

power output. Additionally, higher compression ratios made possible by hydrogen's resistance to knock result in more complete combustion and increased thermal efficiency. Moreover, waste heat recovery systems can harness the high exhaust temperatures generated by dual fuel combustion for supplementary power generation or thermal management, further improving overall efficiency [5].

3. Emissions Mitigation Strategies

In the quest for environmental sustainability, hydrogen-gasoline dual fuel combustion presents a wealth of opportunities for mitigating harmful emissions and reducing the ecological footprint of internal combustion engines. This section explores concrete strategies and technologies aimed at addressing key pollutants and promoting environmental resilience through dual fuel combustion [11, 12].

3.1. Nitrogen Oxides (NO_x) Reduction

Nitrogen oxides (NO_x) emissions pose significant challenges due to their detrimental effects on air quality and human health. Dual fuel combustion offers several pathways for NO_x reduction, including combustion temperature control, exhaust gas recirculation (EGR), and selective catalytic reduction (SCR). By optimizing combustion parameters to lower peak temperatures and employing EGR to dilute the combustion mixture with inert gases, engineers can minimize NO_x formation during combustion. Additionally, SCR systems utilizing ammonia-based catalysts can selectively reduce NO_x emissions to nitrogen and water, further reducing environmental impact [2, 5].

3.2. Particulate Matter (PM) Abatement

Particulate matter (PM) emissions, consisting of fine particles and aerosols, pose significant health risks and contribute to air pollution. Dual fuel combustion can mitigate PM emissions through improved combustion efficiency and particulate filtration technologies. By enhancing combustion stability and promoting more complete fuel oxidation, dual fuel engines generate fewer soot particles and emit lower levels of PM. Additionally, advanced particulate filters and trap systems can capture and remove PM emissions from the exhaust stream, ensuring compliance with stringent emissions standards and safeguarding air quality [1].

3.3. Hydrocarbon (HC) and Carbon Monoxide (CO) Reduction

Hydrocarbon (HC) and carbon monoxide (CO) emissions, resulting from incomplete combustion processes, are key targets for emissions reduction in dual fuel engines. Optimizing air-fuel ratios, combustion phasing, and ignition timing can enhance combustion completeness and minimize HC and CO emissions. Additionally, catalytic converters and oxidation catalysts can oxidize HC and CO pollutants to less harmful compounds, further reducing their environmental impact. By employing synergistic approaches that address multiple pollutants simultaneously, engineers can achieve comprehensive emissions reduction in dual fuel engines [6, 8].

3.4. Greenhouse Gas (GHG) Mitigation

Greenhouse gas (GHG) emissions, primarily carbon dioxide (CO₂), contribute to global warming and climate change. While hydrogen combustion produces no CO₂ emissions, the overall environmental impact of dual fuel combustion depends on the carbon intensity of the primary fuel source. By utilizing renewable hydrogen produced from electrolysis or biomass-derived sources, dual fuel engines can achieve carbon-neutral or even carbon-negative emissions profiles, mitigating their contribution to climate change. Additionally, carbon capture and utilization (CCU) technologies can capture CO₂ emissions from the exhaust stream and sequester them for beneficial reuse, further reducing net GHG emissions [13, 14].

3.5. Regulatory Compliance and Certification

Ensuring regulatory compliance and obtaining emissions certification are critical aspects of emissions mitigation strategies in dual fuel engines. Engineers must design dual fuel systems to meet or exceed stringent emissions standards set by regulatory agencies such as the Environmental Protection Agency (EPA) and the European Union (EU). This involves rigorous emissions testing, validation, and certification processes to demonstrate compliance with emissions limits under real-world driving conditions. By adhering to regulatory requirements and adopting best practices in emissions control, manufacturers can ensure the environmental sustainability and market acceptance of dual fuel engines [15, 16].

4. Future Research Directions

As hydrogen-gasoline dual fuel combustion continues to evolve, ongoing research and development efforts are essential for unlocking its full potential and addressing remaining challenges. This section outlines concrete areas of focus for future research, spanning combustion optimization, fuel infrastructure development, emissions reduction strategies, and advanced propulsion technologies.

4.1. Advanced Combustion Modelling and Simulation

Advancing the state-of-the-art in combustion modelling and simulation is critical for optimizing dual fuel combustion processes and understanding complex combustion phenomena. Future research efforts should focus on developing high-fidelity computational models that accurately capture the interactions between hydrogen and gasoline combustion, as well as the effects of combustion chamber geometry, fuel injection strategies, and turbulence on combustion efficiency and emissions formation. By refining computational tools and methodologies, researchers can gain deeper insights into dual fuel combustion dynamics and accelerate the development of next-generation engines [17, 18].

4.2. Hydrogen Supply

Expanding hydrogen infrastructure is essential for supporting widespread adoption of dual fuel technologies and enabling the transition towards a hydrogen-based transportation ecosystem. Future research should focus on developing cost-effective hydrogen production, storage, and distribution technologies, as well as optimizing hydrogen refueling infrastructure to accommodate dual fuel vehicles. By addressing infrastructure barriers and fostering collaboration between industry stakeholders, researchers can facilitate the deployment of dual fuel technologies and accelerate the transition towards a hydrogen economy [15].

4.3. Green Hydrogen Production Methods

The widespread adoption of dual fuel technologies depends on the availability of renewable hydrogen produced from sustainable sources. Future research should prioritize the development of cost-effective and environmentally friendly methods for renewable hydrogen production, such as electrolysis powered by renewable energy sources, biomass gasification, and photobiological processes. By advancing renewable hydrogen

production technologies, researchers can ensure a sustainable and carbon-neutral fuel supply for dual fuel vehicles, enabling a transition towards a low-carbon transportation future [15].

4.4. Advanced Propulsion Technologies

Exploring advanced propulsion technologies beyond dual fuel combustion is essential for meeting long-term sustainability goals and addressing evolving transportation needs. Future research should investigate alternative powertrain architectures, such as fuel cells, electric hybrids, and hydrogen fuel cell-electric hybrids, that offer complementary benefits to dual fuel combustion, such as zero-emission operation and extended range. By embracing a diverse portfolio of propulsion technologies, researchers can develop integrated solutions that optimize energy efficiency, reduce emissions, and enhance vehicle performance across a range of applications and operating conditions.

5. Applications Across Sectors

5.1. Automotive Propulsion

In the automotive sector, dual fuel technologies have the potential to revolutionize vehicle propulsion, offering cleaner and more efficient alternatives to traditional gasoline engines. Dual fuel engines can be seamlessly integrated into passenger cars, trucks, buses, and commercial vehicles, providing a practical pathway towards decarbonization and emissions reduction. By leveraging hydrogen-gasoline dual fuel combustion, automakers can offer consumers a range of vehicles with improved fuel economy, reduced emissions, and enhanced performance, accelerating the transition towards sustainable mobility.

5.2. Marine Transportation

Marine vessels represent another promising application area for dual fuel engines, particularly in the shipping industry. Dual fuel engines can power a variety of marine vessels, including cargo ships, ferries, and offshore support vessels, offering a cleaner and more sustainable alternative to traditional marine diesel engines. By utilizing hydrogen-gasoline dual fuel combustion, ship operators can reduce emissions of harmful pollutants such as sulfur oxides (SO_x) and nitrogen oxides (NO_x), while also improving fuel efficiency and operational flexibility. Dual fuel propulsion systems enable vessels to switch between hydrogen and gasoline modes, optimizing performance

based on operating conditions and environmental regulations.

5.3. Power Generation

Dual fuel technologies have the potential to transform power generation systems, offering efficient and environmentally friendly solutions for electricity production. Dual fuel engines can be deployed in distributed power generation applications, such as combined heat and power (CHP) systems, microgrids, and backup generators, providing reliable and resilient electricity supply. By harnessing hydrogen-gasoline dual fuel combustion, power generation facilities can reduce emissions of greenhouse gases and criteria pollutants, while also benefiting from improved fuel flexibility and energy security. Dual fuel engines can utilize a variety of fuel sources, including renewable hydrogen produced from electrolysis or biomass-derived sources, enabling a transition towards a more sustainable and decentralized energy infrastructure [19].

5.4. Industrial Perspective

Dual fuel technologies find applications beyond traditional transportation and power generation sectors, extending industrial equipment, and stationary machinery. Dual fuel engines can power construction equipment, agricultural machinery, and mining vehicles, offering cleaner and more efficient alternatives to conventional diesel engines. By adopting hydrogen-gasoline dual fuel combustion, industrial operators can reduce emissions, improve fuel efficiency, and enhance productivity, while also meeting regulatory requirements and sustainability goals. Dual fuel technologies enable the utilization of renewable hydrogen and alternative fuels, paving the way for greener and more sustainable operations across diverse industries [19].

5.5. Aviation and Aerospace

In the aviation and aerospace sectors, dual fuel technologies hold promises for reducing emissions and enhancing fuel efficiency in aircraft propulsion systems. Dual fuel combustion concepts can be applied to aircraft engines, offering a pathway towards decarbonization and sustainability in air transportation. By blending hydrogen with conventional aviation fuels such as jet fuel, dual fuel engines can reduce emissions of greenhouse gases and pollutants, while also improving fuel economy and flight range. Dual fuel propulsion systems enable aircraft to transition towards

cleaner and more sustainable aviation fuels, contributing to the global effort to mitigate climate change and reduce the environmental impact of air travel [20].

6. Conclusion

In conclusion, the hydrogen-gasoline hybrid blending process represents a paradigm shift in the field of internal combustion engines, providing an environmentally friendly, sustainable transition between fossil fuel-free systems and conventional internal combustion engines. By harnessing the collective ingenuity of researchers, engineers, policy makers and industry, we can chart a path to a cleaner, greener and more prosperous future for generations to come.

References

- [1] Purayil S. T. P., Mohammad O. Hamdan, Al-Omari S. A. B., Selim M. Y. E., Elnajjar E.: *Review of hydrogen–gasoline SI dual fuel engines: Engine performance and emission*. Energy Reports, 9. (2023) 4554–4566.
<https://doi.org/10.1016/j.egy.2023.03.054>
- [2] Vasu Kumar, Dhruv Gupta, Naveen Kumar: *Hydrogen use in internal combustion engine: a review*. International Journal of Advanced Culture Technology, 3/2. (2015) 87–99.
<https://doi.org/10.17703/IJACT.2015.3.2.87>
- [3] Joonsuk Kim, Kwang Min Chun, Soonho Song, Hong-Kil Baek, Seung Woo Lee: *Hydrogen use in internal combustion engine. The effects of hydrogen on the combustion, performance, and emissions of a turbo gasoline direct-injection engine with exhaust gas recirculation*. International Journal of Hydrogen Energy, 42/39. (2017) 25074–25087.
<https://doi.org/10.1016/j.ijhydene.2017.08.097>
- [4] Kanga Rui, Zhoua Lei, Huaa Jianxiang, Fenga Dengquan, Weia Haiqiao, Chena Rui: *Experimental investigation on combustion characteristics in dual-fuel dual-injection engine*. Energy Conversion and Management, 181. (2019) 15–25.
<https://doi.org/10.1016/j.enconman.2018.11.057>
- [5] Velmurugan A., Rajamurugan T. V., Rajaganapathy C., Murugapopathi S., Kassian T. T. Amesho: *Enhancing performance, reducing emissions, and optimizing combustion in compression ignition engines through hydrogen, nitrogen, and EGR addition: An experimental study*. International Journal of Hydrogen Energy, 49/2. (2024) 1363–1366.
<https://doi.org/10.1016/j.ijhydene.2024.02.159>
- [6] Das L. M.: *Hydrogen engines: A view of the past and a look into the future*. International Journal of Hydrogen Energy, 15/6. (1990) 425–443.
[https://doi.org/10.1016/0360-3199\(90\)90200-I](https://doi.org/10.1016/0360-3199(90)90200-I)
- [7] White C. M., Steeper R. R., Lutz A. E.: *Hydrogen engines: The hydrogen-fueled internal combustion engine: a technical review*. International Journal of Hydrogen Energy, 31/10. (2006) 1292–1305.
<https://doi.org/10.1016/j.ijhydene.2005.12.001>
- [8] Sun Zehao, Hong Jichao, Zhang Tiezhu, Sun Binbin, Yang Binbin, Lu Liqun, Li Lin, Wu Kaiwei: *Hydrogen engine operation strategies: Recent progress, industrialization challenges, and perspectives*. International Journal of Hydrogen Energy, 48/1. (2023) 366–392.
<https://doi.org/10.1016/j.ijhydene.2022.09.256>
- [9] Ghosh Anupam, Munoz-Munoz Natalia M., Chatelain Karl P., Lacoste Deanna A.: *Laminar burning velocity of hydrogen, methane, ethane, ethylene, and propane flames at near-cryogenic temperatures*. Applications in Energy and Combustion Science, 12. (2022) 110.
<https://doi.org/10.1016/j.jaecs.2022.100094>
- [10] Sementa Paolo, Vargas Antolini Jácson Beltrão de, Cinzia Tornatore, Catapano Francesco, Vaglieco Bianca Maria, López Sánchez José Javier: *Exploring the potentials of lean-burn hydrogen SI engine compared to methane operation*. International Journal of Hydrogen Energy, 47/59. (2022) 25044–25056.
<https://doi.org/10.1016/j.ijhydene.2022.05.250>
- [11] Ugurlu Adem: *An emission analysis study of hydrogen powered vehicles*. International Journal of Hydrogen Energy, 45/50. (2020) 26522–26535.
<https://doi.org/10.1016/j.ijhydene.2020.05.156>
- [12] Hosseini Seyed Ehsan, Wahid Mazlan Abdul: *Hydrogen production from renewable and sustainable energy resources: Promising green energy carrier for clean development*. Renewable and Sustainable Energy Reviews, 57. (2016) 850–866.
<https://doi.org/10.1016/j.rser.2015.12.112>
- [13] Verhelst Sebastian, Wallner Thomas: *Hydrogen-fueled internal combustion engines*. Progress in Energy and Combustion Science, 35/6. (2009) 490–527.
<https://doi.org/10.1016/j.pecs.2009.08.001>
- [14] Gao Jianbing, Wang Xiaochen, Song Panpan, Tian Guohong, Ma Chaochen: *Review of the backfire occurrences and control strategies for port hydrogen injection internal combustion engines*. Fuel, 307. (2022) 121553.
<https://doi.org/10.1016/j.fuel.2021.121553>
- [15] Halde Pobitra, Babaie Meisam, Salek Farhad, Haque Nawshad, Savage Russell, Stevanovic Svetlana, Bodisco Timothy A., Zare Ali: *Advancements in hydrogen production, storage, distribution and refuelling for a sustainable transport sector: Hydrogen fuel cell vehicles*. International Journal of Hydrogen Energy, 55. (2024) 973–1004.
<https://doi.org/10.1016/j.ijhydene.2023.07.204>
- [16] Marcus Newborough, Graham Cooley: *Green hydrogen: water use implications and opportunities*. Fuel Cells Bulletin, 2021/12. (2021) 12–15.
[https://doi.org/10.1016/S1464-2859\(21\)00658-1](https://doi.org/10.1016/S1464-2859(21)00658-1)

- [17] Shravan K. Vudumu, Umit O. Koçlu: *Computational modeling, validation, and utilization for predicting the performance, combustion and emission characteristics of hydrogen IC engines*. Energy, 36/1. (2011) 647–655.
<https://doi.org/10.1016/j.energy.2010.09.051>
- [18] Li Hailin, Karim Ghazi A.: *Knock in spark ignition hydrogen engines*. International Journal of Hydrogen Energy, 29/8. (2004) 859–865.
<https://doi.org/10.1016/j.ijhydene.2003.09.013>
- [19] Hwang Joonsik, Maharjan Krishna, Cho HeeJin: *A review of hydrogen utilization in power generation and transportation sectors: Achievements and future challenges*. International Journal of Hydrogen Energy, 48/74. (2023) 28629–28648.
<https://doi.org/10.1016/j.ijhydene.2023.04.024>
- [20] Yusaf Talal, Shadate Faisal Mahamude Abu, Kadirgama Kumaran, Ramasamy Devarajan, Farhana Kaniz, Dhahad Hayder A., Talib ABD Rahim Abu: *Sustainable hydrogen energy in aviation – A narrative review*. International Journal of Hydrogen Energy, 52/C. (2024) 1026–1045.
<https://doi.org/10.1016/j.ijhydene.2023.02.086>



Investigation of Wear Properties on Duplex Surface-treated 42CrMo4 Steel

Krisztián KORSÓS,¹ Dorina KOVÁCS²

¹ *Budapest University of Technology and Economics, Faculty of Mechanical Engineering, Department of Materials Science and Technology, Budapest, Hungary, krisztian.korsos@edu.bme.hu*

² *Budapest University of Technology and Economics, Faculty of Mechanical Engineering, Department of Materials Science and Technology, Budapest, Hungary, kovacs.dorina@gpk.bme.hu*

Abstract

During the research, 42CrMo4 steel specimens were compared based on surface properties; after three types of duplex surface treatment, and in the untreated state. The treatments included combinations of surface polishing, chemical passivation, and direct current plasma nitriding. The coefficient of friction, wear resistance, and surface hardness properties were determined during the analysis. Scanning electron microscope and stereomicroscope were used to evaluate the results further. Based on the results, it has been proven that all samples with duplex surface treatment in a different way have unique, significantly different surface properties from the other samples, which raises the possibility of widely modifying the surface properties of materials used in industry through the targeted application of duplex surface treatments.

Keywords: *duplex surface treatment, 42CrMo4, direct current plasma nitriding.*

1. Introduction

The continuous development of the technical industry and growth of competitive market demands encourage industrial research specialists to constantly develop existing technologies and develop new technologies, which aim to produce better and higher performance industrial parts and machine components.

If the part in question is exposed to surface stresses, be it mechanical or corrosion, the obvious performance-enhancing technical solution is the targeted modification of the surface of the structure, especially in areas of application where the surface and volume of the part are subject to different stresses.

1.1. Literature review

Plasma nitriding is used in many places to improve the wear resistance of steels due to the compound layer containing iron nitride on the surface and the diffusion zone below it [1, 2]. The passivation of the surface [3, 4] is already a well-established method among stainless steels, by which stains and incipient pitting on the sur-

face caused by environmental corrosion is prevented, but it is also used for other types of steel, as we will cover in the following research.

Molinari et al. [5] investigated the wear properties of 42CrAlMo7 steel specimens treated with gas and plasma nitriding, with particular attention to the different wear behaviour of the diffusion and compound layers. In their research, they found that in the case of a diffusion layer, the microstructural homogeneity of the layer has a greater influence on the friction properties than its hardness. Concerning the compound layer, it was established that thin, non-porous, two-phase surface layers have significantly better friction properties than porous, single-phase compound layers.

Landek et al. [4] performed an examination of the friction and corrosion properties of nitrided, nitrided and phosphated specimens with a composition of 42CrMo4. During their research, they determined, among other things, that a significant improvement in wear resistance can be observed on the test specimen that has undergone plasma nitriding, while the test specimens that have undergone plasma nitriding and phosphating have

a lower wear resistance and coefficient of friction compared to the nitrided one.

Flis [6] attempted passivation of AISI 321 and 431 plasma nitrided steels. As a result of his research, it can be shown that he successfully created, on nitrided test specimens, phosphate and oxide layers that improve both the corrosion properties and, presumably, the wear properties.

Kapuścińska [7] investigated the surface morphology and corrosion properties of nitrided and then phosphated steel with a composition of 42CrMo4. In his research, he found a correlation between the thickness of the formed compound layer and the morphology of the surface phosphate crystals formed during phosphating and established the significant effect of increasing the corrosion resistance of the phosphate layer created on the nitrided layer.

2. Experimental methodology

In the next chapter, we describe the material used in the research, the applied surface treatments and the experimental methods.

2.1. Material

The material chosen for the research is noted as 1.7225 or 42CrMo4. This material is widely used in the automotive industry, with high toughness and an affordable price. Automotive parts, shaft joints, drive shafts, gears and racks are typically made from this type of steel, which is frequently exposed to fatigue, surface wear and friction. Common to all applications is that a targeted modification of the surface properties can greatly increase the service life.

The chemical composition of the steel used in the research, based on the EN 10083 standard, contains the following components: 0.38–0.45 % C, <0.4 % Si, 0.6–0.9 % Mn, <0.025 % P, <0.035 % S, 0.9–1.2 % Cr and 0.15–0.3 % Mn. The raw material was used in the form of $\varnothing 20$ mm round steel, in QT heat treated state and was cut with a water-cooled cutting machine; four test specimens with a thickness of 10 mm were produced.

2.2. The applied surface treatments

Three significantly different surface modification treatments were performed during production of the test specimens. Two of the three available specimens were polished with a 1 μ m grain size polishing paste, two were nitrided for 40 hours at 525 °C in a 1:3 nitrogen-hydrogen atmosphere, and two specimens were cleaned and treated with 10 % HCl solution, after which

pickling in a phosphoric acid medium at 75 °C for 30 minutes was performed. The test specimens are each subjected to two different surface treatments from the three available treatments in such a way that all possible combinations are realized. The specimens that did not undergo polishing, including the reference specimen, were prepared by sanding to a P4000 grain size with gradually decreasing grain size sandpaper before the treatments. The samples produced for the research are listed in **Table 1**.

Table 1. The samples produced for the research

Notation	1. treatment	2. treatment
R	-	-
PF	Polishing	Phosphating
PN	Polishing	Nitriding
NF	Nitriding	Phosphating

2.3. Test methods

After the production of the test specimens, the samples were worn under a load of 5 N, on a 25 m wear path, with a 2 mm diameter carbide ball, without the use of lubricant and with an Anton Paar TRB 3 brand, pin-on-disc type tribometer. During the entire duration of the abrasion, the values of the surface friction coefficient characteristic of the test specimens were registered and then evaluated. After the wear test, the wear track was evaluated with an Olympus SZX16 stereo microscope. The hardness of the samples was determined with a Lynx type Rockwell hardness tester. After the surface tests, the chemical composition of the surface and the wear track, as well as the cross-section images, were examined with a Zeiss EVO MA 10 type scanning electron microscope.

3. Test results

The compound layer formed during nitriding appears as a clearly visible, continuous white layer on the surface (**Figure 1**). Our present research did not examine the thickness, composition, or structure of the layers produced by nitriding or phosphating technology, only the variation in the wear properties caused by the treatment combinations.

3.1. Hardness measurement

We found that a large increase in hardness compared to the reference sample can be observed on the test specimen marked PN. After phosphating in phosphoric acid, a decrease in hardness can be observed on both the PF and NF samples com-

pared to the R and PN samples. These hardness measurement results are illustrated in **Figure 2**.

The decrease in hardness after phosphating is primarily due to the porous surface formed after the treatment (**Figure 3**), while the increase in hardness experienced in the case of nitriding is due to the formed compound and diffusion layer.

3.2. Tribological examination

The results of the tribological tests are illustrated in **Figure 4**.

After plotting the friction coefficient values registered during wear as a function of the sliding distance, the tribological behaviour of the different friction systems can be established in addition to the measurement range and measurement parameters.

The reference sample marked R is characterized by the highest coefficient of static friction, the value of which is 0.56. The gradual reduction of the friction coefficient is the initial run-in period of the friction system, during which the surface roughness is smoothed, and the contact surfaces are formed. After a friction path of 5 meters, the

coefficient seems to stabilize at a value of 0.54.

The sample marked PF, which has undergone polishing and phosphating, has the lowest static friction coefficient of 0.29. During the wear test, a gradual increase in the friction coefficient of the PF sample can be observed, and then, similarly to the R sample, it stabilizes at a value of 0.47 after covering a 5-meter sliding distance.

The sample subjected to polishing and plasma nitriding, marked PN, shows a static friction coefficient of 0.20, but at the same time, a significant increase in its value can be observed within a friction distance of approximately 0 and 5 meters. A gradual decrease in the friction coefficient of the sample can be observed between 5 and 22 meters. The initial sudden value increase and decrease together characterize the run-in period of the sample, during which the gradual decrease from 5 to 22 meters indicates the smoothing and wear of the hard surface roughness peaks on the nitrided surface. At 22 meters, the sample reaches its constant wear coefficient of 0.59.

The sample, noted as NF, shows an initial static friction coefficient value of 0.38. The friction coef-

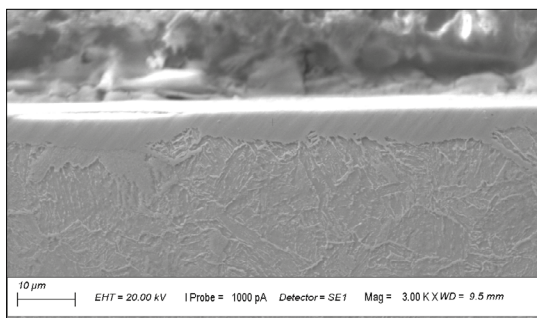


Fig. 1. Compound layer present on the sample marked PN.

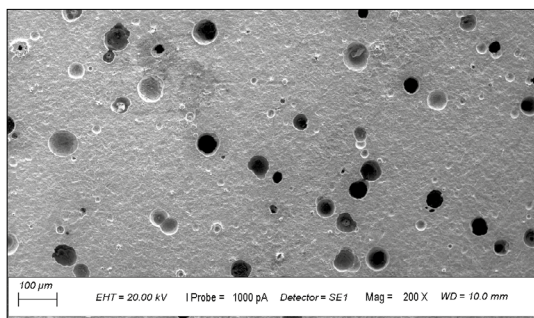


Fig. 3. Surface pores formed on sample PF.

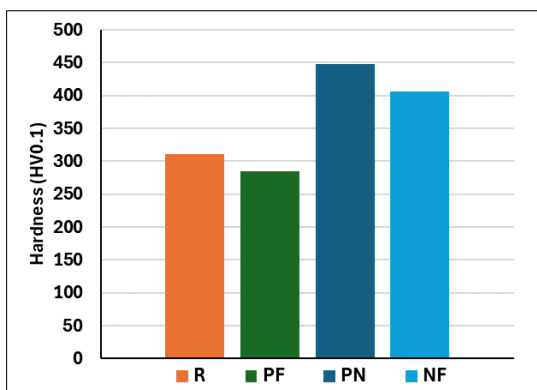


Fig. 2. Hardness values of the samples.

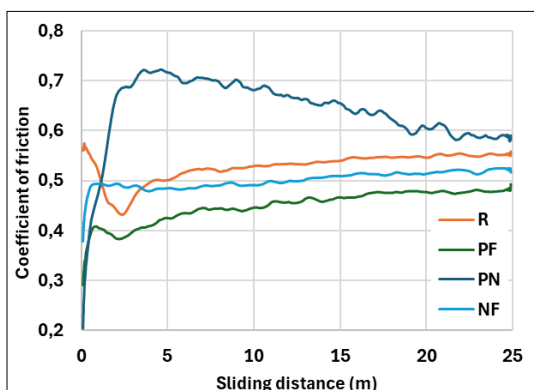


Fig. 4. The results of the tribological tests.

ficient of the sample stabilizes at an average value of 0.50 after only 1 meter.

It can be noted that plasma nitriding greatly increases the surface friction coefficient during the run-in period and causes a notable increase in the steady-state coefficient compared to the reference sample. Phosphating basically reduces both the static and steady-state friction coefficients compared to the reference sample. The combined application of nitriding and phosphating results in a reduced run-in and steady-state friction coefficient compared to the reference and plasma nitrided sample. On sample NF, wear debris clogged pores can be observed, which further decreased the friction coefficient of the sample **Figure 5**.

3.4. Abrasion resistance tests

The wear volumes were determined by knowing the width and length of the wear tracks and the diameter of the wear ball. The measurement results are illustrated in **Figure 6**.

Regarding the results, it can be concluded that the wear resistance shows a correlation with the surface hardness values. The sample marked PN has the smallest wear volume, while a proportional increase in hardness can be observed in the case of the NF sample. A slight increase can also be observed in the phosphatized sample compared to the reference sample.

5. Conclusions

During the measurement results, it can be established that phosphating as a secondary surface treatment can reduce the friction coefficient of the base surface, but at the same time, it reduces its wear resistance. It can be observed that after

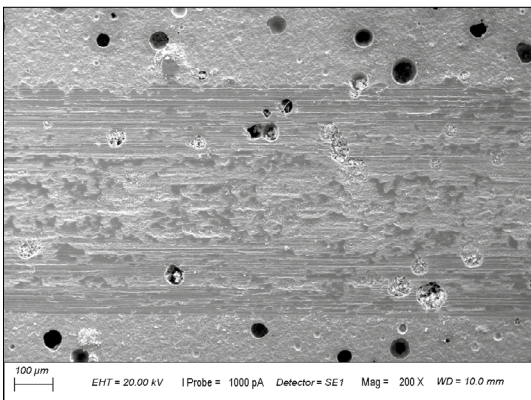


Fig. 5. Pores filled with wear debris found in the wear track of sample PF.

the passivation of the nitrided samples, the improvement in the value of the coefficient of friction is significantly greater than the visible decrease in the hardness value. The surface layers created by phosphating showed an outstanding coefficient of friction in both cases.

At the same time, deterioration is observed after phosphating in terms of hardness and wear resistance properties. As a result of the research, it can be concluded that the duplex layer produced by plasma nitriding and surface treatment in a phosphoric acid medium shows a significant improvement in both friction coefficients compared to the reference and plasma nitrided samples, while at the same time, an improvement can be observed in the wear resistance of the duplex surface treatment sample compared to the reference and phosphated samples.

Acknowledgement

This work was supported by the National Research, Development and Innovation Office (NKFIH) under grant contract OTKA-PD_21 142307.

This project was also supported by the Doctoral Excellence Fellowship Programme (DCEP) is funded by the National Research Development and Innovation Fund of the Ministry of Culture and Innovation and the Budapest University of Technology and Economics, under a grant agreement with the National Research, Development and Innovation Office.

References

- [1] Szilágyiné B. A.: *Active Screen Plasma Nitriding - State of the Art*. Production Processes and Systems, 7. (2014) 103–114.
- [2] Ni J., Ma H., Wei W, An X, Yu M., Hu J.: *Novel Effect of Post-Oxidation on the Comprehensive Perform-*

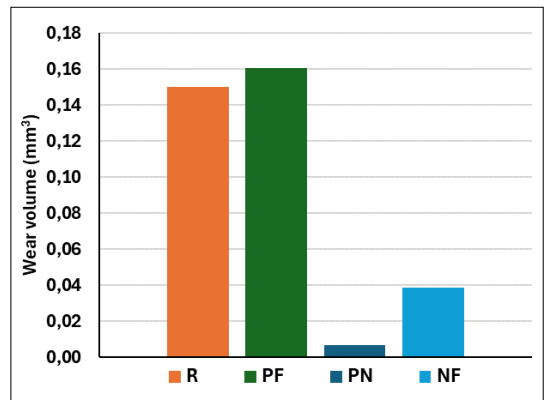


Fig. 6. The results of the wear resistance test.

- mance of Plasma Nitriding Layer. *Coatings*, 14/1. (2024) 86.
<https://doi.org/10.3390/coatings14010086>
- [3] Kusmic D., Thanh D., Hruby V.: *Corrosion and Wear Resistance of Plasma Nitrided and Duplex Treated 42CrMo4 Steel*. *Manufacturing Technology*, 18. (2018) 259–265.
<https://doi.org/10.21062/ujep/88.2018/a/1213-2489/MT/18/2/259>
- [4] Landek D., Kurtela M., Stojanović I., Jačan J., Jakovljević S.: *Corrosion and Micro-Abrasion Properties of an AISI 316L Austenitic Stainless Steel after Low-Temperature Plasma Nitriding*. *Coatings*, 13/11. (2023) 1854.
<https://doi.org/10.3390/coatings13111854>
- [5] Molinari A., Straffelini G., Pellizzari M., Pirovano M.: *Wear behaviour of diffusion and compound layers in nitrided steels*. *Surface Engineering*, 489–496. (1998) 6–14.
<https://doi.org/10.1179/sur.1998.14.6.489>
- [6] Flis J.: *Corrosion and passivation of plasma nitrided stainless steels*. *Surface Engineering*, 26. (2010) 103–113.
- [7] Kapuścińska A., Kwiatkowski L., Wach P., Mazurek A., Diduszko R.: *Anticorrosion Properties and Morphology of Phosphate Coating Formed on Nitrided Surface of 42CrMo4 Steel*. *Archives of Metallurgy and Materials*, (2020) 65.
<https://doi.org/10.24425/amm.2020.131749>



Effect of Cutting Gases on the Hardness of Thermally Cut High Strength Steels

János KUTI,¹ Enikő Réka FÁBIÁN,² József GÁTI³

¹ Óbuda University, Doctoral School on Materials Sciences and Technologies, Budapest, Hungary
kuti.janos@gmail.com

² Óbuda University, Bánki Donát Faculty of Mechanical and Safety Engineering Faculty, Institute of Materials and Manufacturing Sciences, Department of Material Technology, Budapest, Hungary,
fabian.reka@bgk.uni-obuda.hu . 2

³ Óbuda University, Bánki Donát Faculty of Mechanical and Safety Engineering University Research and Innovation Center, Budapest, Hungary, gati.jozsef@bgk.uni-obuda.hu

Abstract

In this work, it was illustrating the consequences of flame cutting on XAR® 400 and S960Q type high-strength steels. During flame cutting, the metal, locally heated to ignition temperature, burns in the oxygen beam and removes the resulting combustion product from the kerf. As a result of the process, chemical and physical changes occur in the microstructure of the steel, which can have a significant effect on its properties. Examining the microstructural transformations due to flame cutting of high-strength steels is essential from the point of view of proper design and production. In case of XAR® 400 steel quality, increasing the cutting oxygen significantly changes the microstructure, with a high reduction in hardness in the heat affected zone at cutting zone. For S960Q steel, flame cutting does not cause a drastic change in the microstructure of steel, and increasing the amount of cutting oxygen does not significantly change the hardness.

Keywords: *flame cutting, hardening, high strength steel.*

1. Introduction

Nowadays, high-strength and high strength steels are becoming increasingly popular [1, 2]. The main driving force is the need to reduce the mass of the structure. After all, from the material with higher mechanical properties, a smaller section cross section or wall thickness is enough to bear the same load. Since the density of structural and increased strength steels is almost identical, it can be seen that the weight of structures and vehicles built in this way will be less with the same strength [3, 4].

When manufacturing structures, these steels have to be cut and sometimes welded. The cold working methods, shearing and punching, can be used up to a plate thickness of about 10 mm and are mainly limited to the softer structural steels [5]. High strength steels can typically be processed by thermal cutting, but especially in thick plates, a number of microstructural changes can

occur. Sometimes cracking at the cut edges [5].

XAR 400 steel, produced by Thyssen Krupp Steel, is characterised in particular by high wear resistance and good impact strength, as well as good bending and welding properties. Plates of the XAR® 400 grade receive the required properties as a result of austenitizing and follow-on quenching in special facilities and where applicable, tempering below Ar1. Its main applications are in maintenance, metallurgy, energy industry, coal and cement production [6].

SSAB's tempered high-strength steel S960QL owes its high strength characteristics to its alloying content and heat treatment (two-cycle) consisting of hot rolling hardening (Q) and high temperature tempering (HTT).

In the case of thermal cutting of high strength steels, as in welding, changes in the microstructure occur. It is known from the literature that when high strength steels are welded, the micro-

structure and consequently the hardness in the heat affected zone changes [7, 8]. High strength steels show a higher sensitivity to welding and cutting heat input compared to conventional structural steels. While in low or medium strength steels the HAZ toughness and hardness can be significantly affected by the $t_{8/5}$ cooling time, in S960QL significant hardening and toughness reduction was observed in the whole cooling time range of the most common arc welding processes $t_{8/5} = 2.5\text{--}30\text{ s}$. In case of $t_{8/5} = 100\text{ s}$ softening and extremely low Charpy V-notch impact test values were identified [9].

The question arises: what happens in the area around the cut edge when cutting thick plates? How will the cutting technology affect the vicinity of the cut edge?

2. Materials and Testing

For the experiments, micro alloyed and fine-grained high-strength steels of type XAR[®]400 and S960Q were flame cut. The nominal composition of XAR[®]400 steel is: C = 0.14 %, Si = 0.22 %, Mn = 1.14 %, Al = 0.1 %, B = 0.002 %, P = 0.01 %, S = 0.001 %, Cr = 0.23 %, Mo = 0.01 %, Nb = 0.02 %, Ti = 0.05 % [10].

The nominal composition of S960Q steel is: C = 0.16 %, Si = 0.2 %, Mn = 1.22 %, Cr = 0.2 %, Ni = 0.05 %, P = 0.011 %, S = 0.01 % [11].

Different thicknesses of steel plates were used in the tests. The measurements were carried out on steel plates with a thickness of 8 mm for XAR[®]400 and 10 mm for S960 Q. Microstructure of the studied steels is shown in Figure 1.

For our experiments, 300 mm long test pieces were cut at Linde Hungary Zrt.'s Budapest site for both high strength steels.

The technological data are shown in Table 1.

In case of the manual cutting gun there was an oxygen feed, in the machine cutting gun there was a separate heater and cutter oxygen feed, the burner design was head-mixed.

In the case of the flame cutting process, the flame heats the material at the surface until its ignition temperature is reached. In addition, oxygen is blown into the kerf. At this point the material starts to burn, and the cutting process begins. Thereafter, the combustion releases further heat. This in turn heats the underlying material up to ignition temperature. This allows the process to continue automatically into the depths. The metal oxides are blown out of the kerf together with the cutting oxygen.

The used cutting gases physical properties differ between them. The flame temperature in case of acetylene can achieve $\approx 3200^\circ\text{C}$ in oxygen and $\approx 2100^\circ\text{C}$ in air (see Table 2). Such a high temperature makes faster piercing and cutting possible.

At the same time, acetylene's secondary flame temperature is comparatively low. Propane can reach quite high temperatures. The maximum is around 2800°C . Compared to acetylene, the concentration of the flame is smaller, resulting in a larger HAZ and longer piercing time. The cutting speed is comparable, though. The ratio of oxygen to propane is around 4.3:1. Thus, reaching the maximum temperature requires around 3.5 times more oxygen than oxy-acetylene cutting [12].

2.1. Preparation of specimens

After the cutting process, for each flame cut the changes in microstructure at the beginning of the cuts was investigated, in the middle of the cuts and at the end of the cut edge vicinities. For metallo-

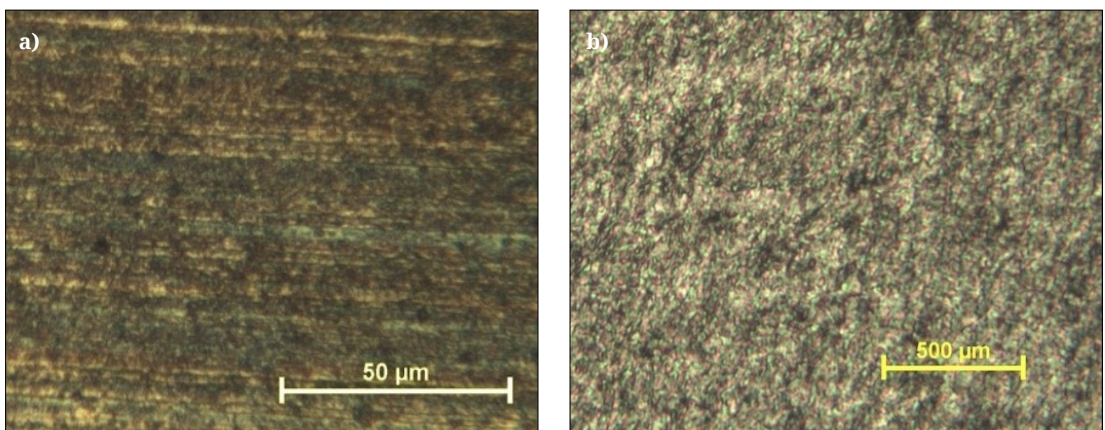


Fig. 1. The microstructure of the tested steel plates a) XAR[®]400 b) Q960.

Table 1. Sample notification and technological data

Sample	Nozzle	burner/ fuel	$P_{O_2 \text{ Heat}}$	$P_{O_2 \text{ cut}}$	P_{CH}	$V_{O_2 \text{ Heat}}$	$V_{O_2 \text{ cut}}$	V_{CH}	v	l	kerf
			bar			L/h			cm/min	mm	
CAK	ANME10-30	C_2H_2	4	4	0,5	700	1500	350	48	10	
CPK	HP337	C_3H_8/O_2	3	4	0,5	600	1450	200	33	11	1.6
CAG	ANME10-30	C_2H_2	2	4	0,5	400	2400	350	58	8	
CPG	PNME10-25	C_3H_8/O_2	2	3	0,5	400	1200	200	36	10	1.7
DAG	ANME10-30	C_2H_2	2	4	0,5	400	2400	350	46	8	
DPG	PNME10-25	C_3H_8/O_2	2	3	0,5	400	1200	200	34	10	1.7

Markings used:

- first character: material quality (C- XAR®400/8; D – S960 Q/10),
- second character: gas (A: acetylene, P: propane),
- third character: G: „mechanical” (separate heating and cutting oxygen feed, mixing torch design), K: manual (one O_2 feed),

Nozzle – nozzle factory mark, for traceability,

- burner/fuel – gas combination used for the preheating flame,
- $P_{O_2 \text{ Heat}}$ (bar) – pressure of oxygen gas used for preheating flame,

- $P_{O_2 \text{ Cut}}$ (bar) – cutting oxygen pressure,
- P_{CH} (bar) – pressure of combustible gas,
- $V_{O_2 \text{ Heat}}$ (l/h) is the amount of oxygen used for the preheating flame,
- $V_{O_2 \text{ Cut}}$ (l/h) is the amount of oxygen used for cutting,
- V_{CH} (l/h) is the quantity of combustible gas,
- v (cm/min) is the cutting speed,
- l (mm) is the distance between the burner and the workpiece,
- kerf (mm) size of cut gap.

Table 2. Main physical properties of fuel gases

Characteristics	Propane	Acetylene
	C_3H_8	C_2H_2
Density at 15 °C, 0.1 MPa, (kg/m ³)	1.87	1.171
Density in comparison to air (air=1)	1.55	0.9
Ignition point in air, (°C)	466	335
Ignition limit, (V%)		
In air	2.1–9.5	3–82
In oxygen	2.0–48	3–93
Flame power, (W/mm ²)	104.5	448
Flame temperature, (°C)		
In air	1920	2100
In oxygen	2780	3126
Heating rate, (kJ/m ³)	92000	56800

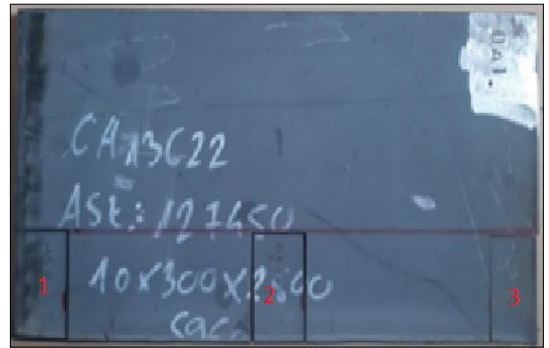


Fig. 2. Cutting arrangement of samples: „1” specimen - start of cutting, „2” sample - middle of cutting, „3” sample - end of cutting

graphic study the sample were cut by the waterjet cutting technique at Woldem Ltd. The cutting design is illustrated in **Figure 2**: the first sample was cut at the beginning of the plate, then in the middle and at the end. The use of waterjet cutting was also necessary to avoid heat exposure to the pieces during cutting.

After water jet cutting, samples cut from the same sheet were simultaneously cold-embedded using two-component Duracryl plus acrylic

resin. After solidification of the acrylic resin, the samples were prepared using increasingly finer grinding paper (P60, P 100, P 220, P 400, P 600, P 1200) and polished with 3 μ m and 1 μ m diamond paste at Buehler Ecomet 250 Pro equipment. The microstructure changes were studied after etching with Nital-e etchant.

The hardness distribution of the samples was determined with Buhler Wilson W 3111S by HV 5 hardness measurement. The indentation distance

in the immediate vicinity of the cutting edge and in the heat affected zone was 1 mm and outside of the heat affected zone was 5 mm.

For the examination and evaluation of the hardness indentation, Zeiss Axio Observer Z1m optical microscope and the associated computer software were used.

3. Results

It was investigated if there is a difference between manual cutting and mechanical cutting. In our experiments, the effect of the quality of the burner gases (acetylene or propane) was studied, while their pressure was kept at the same value.

3.1. Microstructural changes in case of flame cutting of XAR[®]400 steel plates

In case of XAR[®]400 steel plate cutting, it was found that microstructure changes occur near the cutting edge in each case, when various fuel gases were applied. About 100 μm thick decarburized layer was observed near the cut edge, as it is visible at [Figure 3](#).

For XAR400 steel, hardness measurements near the cut edge show that the effects of propane and acetylene were similar at the beginning ([Figure 4](#)), middle ([Figure 5](#)), and end ([Figure 6](#)), of the cut edge when applied by hand torch, but differed when the machine torch was operated ([Figure 7](#)).

Towards to the end of the cutting zone, softened thickness exceeds 5 mm (the hardness is less than 300HV5). When cutting were effectuated with propane, this material softened layer thickness was lower than when acetylene was applied in case of manual cutting work ([Figure 6](#)).

Studying the [Figures 4.](#), [5.](#) and [6.](#) it can be concluded that the hardness values in the immediate vicinity of the cutting edge are more favourable using propane fuel gas, although the differences cannot be said to be drastic. Away from the cutting edge, the hardness sets to almost the same value. The different hardness values near the cutting edge may be explained by the flame power differences. Acetylene has a much higher flame power (448 W/mm^2) than propane (104.5 W/mm^2), so grain coarsening appearance is more likely near the cutting edge, resulting in deterioration of hardness values.

When using a machine torch, acetylene caused more pronounced softening on the cutting edge of the plate at the outer 5mm than propane, and the softened zone is clearly wider than when using a manual torch ([Figure 7.](#)).

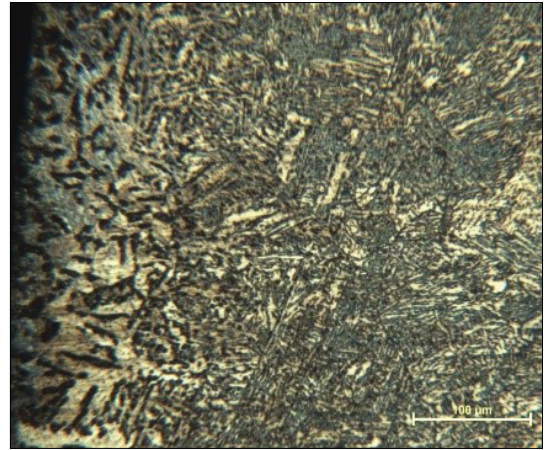


Fig. 3. Microstructural change in the cutting vicinity in the case of XAR 400 steel plate.

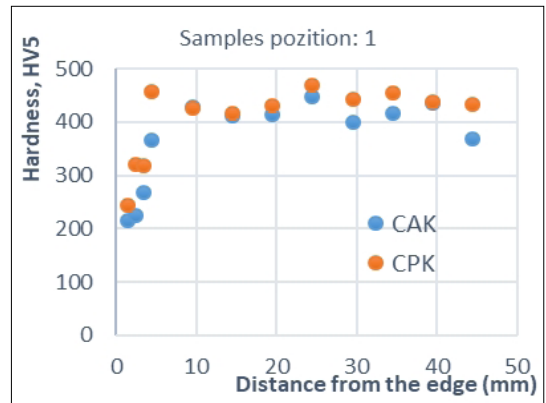


Fig. 4. Hardness variation from the cutting edge for CAK/CPK pieces at the beginning of the cutting. Manual torch.

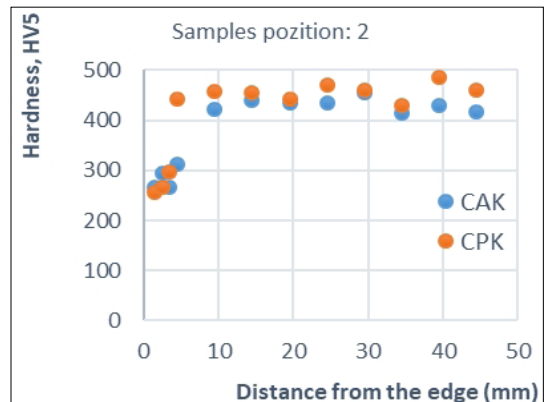


Fig. 5. Hardness variation from the cutting edge to the inside of the sample for CAK/CPK pieces at the middle of the cutting. Manual torch.

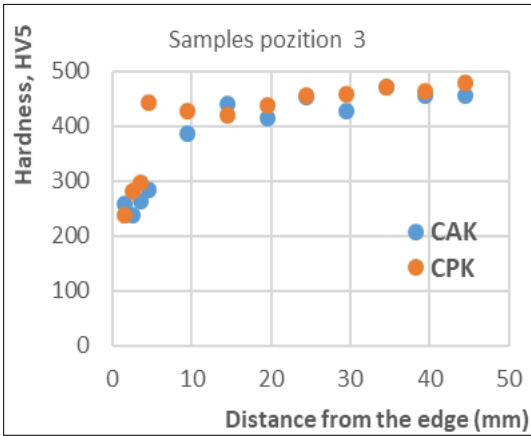


Fig. 6. Hardness variation from the cutting edge to the inside of the sample for CAK/CPK pieces at the end of the cutting. Manual torch.

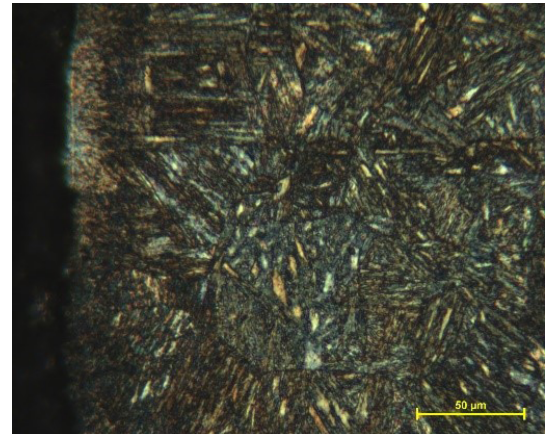


Fig. 9. Microstructure of 960Q steel plate near the cutting edge.

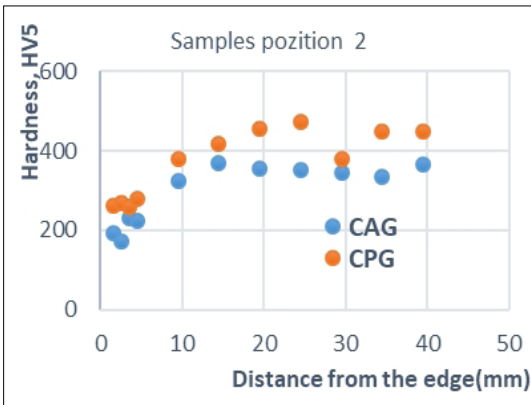


Fig. 7. Hardness variation from the cutting edge to the inside of the sample for mechanically cut CAG/CPG pieces at the middle of the cutting.

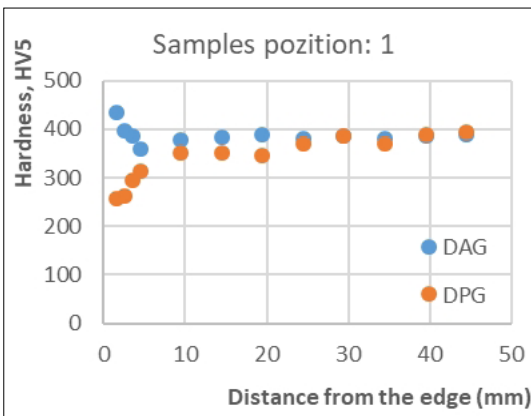


Fig. 8. Hardness variation from the cutting edge to the inside of the sample for mechanically cut S960Q steel plate (DAG/DPG pieces).

3.2. Effects of different fuel gases on the microstructure of S960Q steel plate during cutting

The effects of propane and acetylene differ significantly for 960Q steel grades. While acetylene caused an increase in hardness at the outer 5 mm of the cut edge, propane caused a softening of this zone, as shown in [Figure 8](#). Moving away from the cutting edge, the hardness values of the two samples are almost identical.

Examining the microstructure of the steel, a 10 μm thick layer of melted and re-solidified material was observed in the vicinity of the cut edge. Within it, bainite formed from coarse-grained primary austenite can be seen ([Figure 9](#)). Right next to the cutting edge, it can be observed that the material has been melted. As a result of melting, the formation of some dendritic tissue can be seen at a large ki thickness.

4. Conclusion

Based on the results and experience summarised in the article, the following main conclusions can be made:

1. XAR400 steel grade is not recommended to be cut by flame cutting process. The microstructure can be transformed at great depths under the influence of the flame, thereby also reducing the hardness values.
2. For XAR400 steel grade, increasing cutting oxygen caused a decarburization in microstructure and the greatest decrease in hardness.
3. Basing on the results the S960Q steel grade can be properly cut by flame cutting process. The cut does not cause drastic changes in micro-

structure. The sample recrystallizes, but the recrystallized zone is small enough to be reprocessed or removed by a slight post-processing during post-cut welding.

4. With regard to S960Q steel grade, no change in cutting oxygen quantity can be observed being significant in terms of hardness as in the XAR400 steel grade.

References

- [1] Gáspár M. Gy.: *Nemesített nagyszilárdságú acélok hegesztésének nehézségei*. TDK-dolgozat, Miskolc, 2010.
- [2] Komócsin M.: *Nagyszilárdságú acélok és hegeszthetőségük*. Gépgyártás, 41/11. (2002) 24–29.
- [3] Béres G., Danyi J., Végvári F., Tisza M.: *Napjaink járműkarosszéria anyagai*. Gradus, 2/2. (2015) 209–224.
- [4] Zhang W., Xu J.: *Advanced lightweight materials for Automobiles: A review*. Materials & Design 221. (2022) 110994. <https://doi.org/10.1016/j.matdes.2022.110994>
- [5] TECHSUPPORT #16 Thermal Cutting of Hardox and Wieldox. <https://www.australiansteel.com.au/wp/wp-content/uploads/2015/09/Cutting-of-Hardox-Wear-Plate.pdf> (accessed on: 2024. nov. 7.)
- [6] XAR®400 acéllemez <https://www.flinkenberg.fi/wp-content/uploads/DATASHEET-XAR400.pdf> (accessed on: 2024. sep. 9.)
- [7] Mihályfi T.: *Undermatching elven választott hozaganyag hatásának elemzése nagyszilárdságú acélok hegesztésekor*. Diplomamunka, Miskolci Egyetem, Anyagszerkezetani és Anyagtechnológiai Intézet, Miskolc, 2014.
- [8] Gáspár M., Balogh A.: *GMAW experiments for advanced (Q+T) high strength steels*. Journal of Production Processes and Systems, 6/1. (2013) 9–24.
- [9] Gáspár M.: *Effect of Welding Heat Input on Simulated HAZ Areas in S960QL High Strength Steel*. Metals, 9/11. (2019), 1226. <https://doi.org/10.3390/met9111226>
- [10] Thyssen Krupp Steel Europe: XAR400 TKS-WBL 703 06.10
- [11] MSZ EN 10025-6: Melegen hengerelt termékek szerkezeti acélokból. 6. rész: Nagy folyáshatárú szerkezeti acélokból készült, nemesített lapos termékek műszaki szállítási feltételei (2019+A1:2023)
- [12] Fuel gases for oxyfuel cutting <https://fractory.com/fuel-gases-for-oxyfuel-cutting> (accessed on: 2024. oct. 12.)



The Effect of Surface Machining Design on the Efficiency of Laser Surface Treatment

Béla MÉSZÁROS,¹ Enikő Réka FÁBIÁN²

¹ Óbuda University, Bánki Donát Faculty of Mechanical and Safety Engineering Faculty, Institute of Materials and Manufacturing Sciences, Department of Manufacturing Technology, Budapest, Hungary
meszaros.bela@bgk.uni-obuda.hu

² Óbuda University, Bánki Donát Faculty of Mechanical and Safety Engineering Faculty, Institute of Materials and Manufacturing Sciences, Department of Material Technology, Budapest, Hungary,
fabian.reka@bgk.uni-obuda.hu

Abstract

Laser surface treatment is increasingly used for surface hardening. In this series of experiments we studied the milling groove design effect on laser hardened surfaces at 42CrMo4 steel after corresponding laser parameters. Milled grooves of 0.25 mm, 0.50 mm and 0.75 mm depth were studied. The used diode laser and its set parameters had the same focus distance in all cases; however, the power and travel speed of the laser light were changed according to the previously developed experimental plan. Higher laser heat input resulted in a deeper hardened zone. The 45° V-profile milling, and hence the 45° angles of incidence of the laser beam increased the thickness of the hardened layer. The deepest hardened layers were formed at the highest specific heat input and at the deepest grooves.

Keywords: 42CrMo4 steel, diode laser, laser surface heat treatment, milling groove design.

1. Introduction

Surface heat treatment of structural materials and shafts is a common practice in the industry today, in order to create durable, wear-resistant surfaces and edges. A common requirement is the use of a material whose microstructure can be made tough in the core and whose surface can be made hard and wear-resistant by a surface treatment process.

In the past, flame hardening has been used for individual production of case hardenable steels due to cost implications, while induction hardening has been used for large series to produce a thicker wear-resistant layer. Flame hardening does not necessarily produce uniform thickness for surface hardened layers.

In case of induction heat treatment, the thickness of the hardened layer also depends on the air gap between the inductor and the material surface. Grooves formed by milling are typically designed such that it is difficult to form the inductor with an uniform air gap.

The basic principle of laser surface treatment is the same as for any heat treatment process, which is to change the microstructure of the material by heating the steel to austenitic state and then rapidly cooling the material to achieve a martensitic microstructure [1, 2]. The thickness of the hardened layer formed on the surfaces as a result of laser treatment depends on the material of the workpiece (the effect of the alloying agents). The amount of heat input (energy absorbed) during laser treatment depends on the surface quality of the workpiece, the surface design and the angle of incidence of the beam on the surface. The size of the workpiece determines how much heat can be absorbed by the workpiece. In the case of laser heat treatment, the thickness of the hardened layer that can be created depends on the speed of the laser head, the distribution of the laser power and the wavelength of the laser light [3, 4]. Based on the literature data [5, 6], the reflection of CO₂ lasers with a wavelength of 10,64 μm on polished materials is typically above 90 %, but can be reduced to 20 % by surface roughening. The litera-

ture shows that the effect of surface roughness on the absorption of the laser beam is not as significant in case of solid-state lasers and diode lasers as in the case of CO₂ lasers [6, 7] (Table 1).

Table 1. Absorption coefficient at different surface qualities and laser technologies [6]

Surface	Absorption, %	
	CO ₂ laser, 10600 nm	Nd:YAG laser, 1064 nm
Polished	4	30
Turned	5–7	33–37
Sandblasted	6–8	36–43
Oxidised	21–23	46–51
Graphitised	60–80	60–80
Polished	70–80	70–80

While it can be seen in Table 1 that a rougher surface has a better absorption, conventional roughness values such as Ra, Rq and Rz are not suitable for directly predicting the absorption capacity of a metal surface. There are examples in the literature [8] where similar roughness values have shown different absorptivity. Bergström [9] proposed to use the mean slope of the surface profile instead of surface roughness values to describe the absorptivity.

According to Kügler [10], the dependence of laser beam absorption on surface roughness differs for different steel grades. The hybrid roughness value, Sdq, which is the root mean square gradient and therefore close to the proposal of Bergström [9], seems not to be suitable for absorptivity predictions for the stainless steel (1.4301) and the tool steel (1.2344). For the spring steel (1.1248), there is a certain dependency. Regarding hardenability, spring steels and quality steels are comparable. The ideal hardenable section diameter can be calculated by Grossmann formula [11, 12]

According to the MSZ EN ISO 683-2:2018 standard the 42CrMo4 (1.7225) steel grade is widely used in industry because of its excellent machinability and good heat treatability. Due to its chromium and molybdenum content, it is a typical material for extremely tough, heavy-duty machine parts. It has 46 W/mK thermal conductivity. Its mechanical properties can be varied over a wide range with the aid of heat treatment [13].

Dewi et al [14] have studied the effect of laser beam angle of incidence (10°, 20°, 30°) on similar medium carbon steels (38MnSiVS5 and 44Mn-SiVS6). It was found that scanning the surface

at constant speed but with higher angles of incidence resulted in a higher degree of indentation, but was material quality dependent.

The question arises as to how the grooves formed by different milling methods affect surface hardening. In our experiments, we studied how grooves made to a depth of 0.25 mm; 0.5 mm; 0.75 mm affect the laser hardening depth layer in the case of pre-hardened 42CrMo4 grade steel when diode lasers are applied.

2. Materials and technology

The applied material was a pre-hardened 42CrMo4 steel bar (C= 0.41 %, Si= 0.3 %, Mn =0.7 %, Cr =1.1 %, Mo=0.2 %). with 305HV2 hardness. The dimensions of the bar were 50×50×200 mm.

The aim of the experiments was to investigate the thickness of the hardened surface created by the diode laser on surfaces of different shapes. Based on preliminary literature research, we decided to produce „V” shaped grooves. For the groove milling, we needed a tool that could machine the surfaces with the right precision and to the right depth. The used technology was milling and the used milling tool was a solid carbide end mill tool (MC326-12.0W4L050C-WK40TF) with a 90° entering angle (KAPR), which created „V” shaped grooves in the surface.

The main parameters of the tool were: z=4 teeth, D= Ø12 mm. The tool constitution is fine-grained carbide. The coating used was TiAlN. The tool creates a R 0.5 mm radius at the bottom of the „V” shaped grooves. In the case of side milling, the 50° helix angle cannot be neglected either, but since our largest infeed is 0.75 mm, the effect of this parameter on cutting is negligible. The applied cutting parameters were the same for all „V” shaped grooves. However, we must note that our cutting speed approaches zero at the axis line of the tool, but the maximum depth of the „V” shaped grooves of 0.75 mm mean that the change in cutting speed is negligible in this case. The set cutting speed was Vc=32 m/min and the feed rate was f=74 mm/min. The cutting parameters were defined based on tool catalogue data. The most important element of the present experiment is the infeed, which in all cases was the same as the depth of the „V” shaped grooves, the machining angle was 45° These infeed and groove depths were as follows, 0.25; 0.5; 0.75 mm (Figure 1).

It is important to point out that in all milling operations a MOL Emolin 505 of cooling-lubricating fluid was used, thus reducing the amount of heat

introduced onto the surfaces and resulting in no changes in the microstructure.

The laser annealing of the surfaces was carried out at the Budai Benefit Laser Technology Ltd., where a 4kW diode laser was used, with three different technological data pairs. A focal length of 340 mm was used for the experiments.

Based on preliminary literature data, 150 Ws/mm, 200 Ws/mm and 240 Ws/mm specific laser heat input were used in the heat treatment of the sample surfaces.

The technological data for each sample designation is shown in **Table 2**.

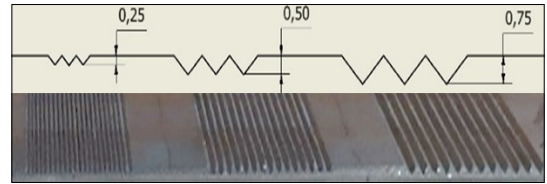
The surface-treated specimen was sawn off with a band saw at a thickness of 10 mm near the heat-treated surface using a cooling-quenching liquid. For metallographic analysis from the sawed plates were cut 40 mm wide samples at the center lines of the heat-treated strips, in such way to allow study of both the milled groove portion and the flat surface zone (**Figure 2**).

The samples were embedded perpendicular to the heat-treated surfaces in two component epoxy resin. After grinding and polishing several ranges the samples were etched by 2 % Nital. In this way the microstructure of samples can be analysed. The microstructure of the hardened layers were studied using an Olympus DSX 1000 tip digital light microscope.

The hardness of samples was measured by Zwick 3212 hardness testing apparatus. The hardness evolution from the surface to the inside of the steel samples was taken perpendicular to the plane surfaces. At heat treated milled grooves the hardness measurements were positioned in middle of grooves. In order to measure hardness respecting the prescribed spacing between the indentations [15],], the load was designed to be 1.962 N.

3. Results

On the metallographic specimens, we found that even at the lowest specific laser heat input, the milled groove surroundings were more deeply hardened than at the flat surfaces. Even at the smallest energy input per unit length, it is striking that the surface where the angle of incidence of the laser beam with the surface is 45° (even at the first groove) has a deeper heat treated layer than the flat surfaces where the angle of incidence of the laser beam is perpendicular to the surface (**Figure 3**).



1. ábra. Az elkészített felületek vázlata és képe

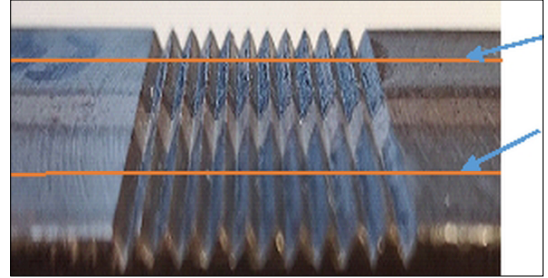


Fig. 2. The appearance of 0.75 mm deep milling grooves after heat treatment The arrows show the position of the metallographic samples cutting line.

Table 2. Technological parameters for samples

Laser parameters	Sample numbers and the milling groove size		
	0.25 mm	0.5 mm	0.75 mm
1.2 kW → 8 mm/s	1	2	3
1.6 kW → 8 mm/s	4	5	6
1.2 kW → 5 mm/s	7	8	9

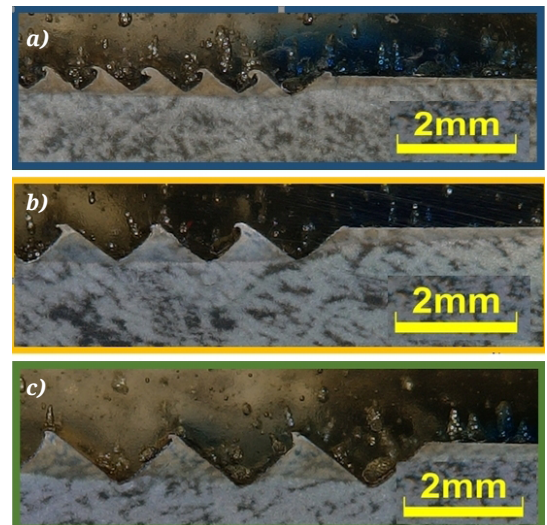


Fig. 3. Micrographs after heat treatment with 150 Ws/mm specific heat input a) sample nr. 1 b) sample nr. 2 c) sample nr. 2.

In agreement with the metallographic micrographs, the hardness variation plots show that the depth of the V-grooves created by milling increases the depth hardened layers on the machined parts. In the full depth of the teeth, the hardness exceeded 700 HV0,2 (Figure 4).

The deeper the grooves, the deeper the hardened surface layer occurred. The hardness measurements results suggest that the hardened surface layers are martensitic. The metallographic studies clearly confirm this, when high resolutions were applied (Figure 5).

Increasing the laser beam power from 1200 W to 1600 W and staying at 8 mm/s travel speed (200 s/mm

specific heat input), the hardened layer thickness increased significantly, especially in the vicinity of the milling grooves (Figure 6).

In this case, when the specific heat input was 200 W s/mm, martensitic microstructure was found below the flat surfaces up to 350 μm. In the zone where grooves were created by milling, the surface modification depth increased. Hardness measurements show that the hardened layer thickness was more than 850 μm for the 0.25 mm and 0.5 mm grooves, while it exceeded 1000 μm for the 0.75 mm groove depth (Figure 7).

Comparing to the first set of samples, keeping

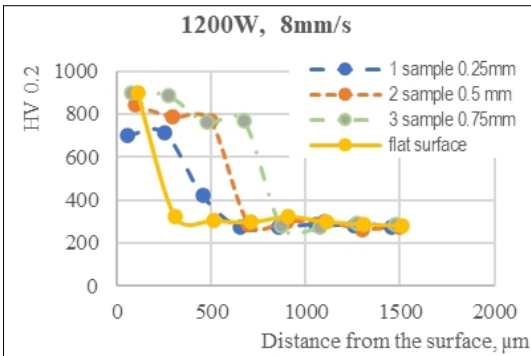


Fig. 4. Hardness as a function of depth in the case of 150 W s/mm specific laser heat input.

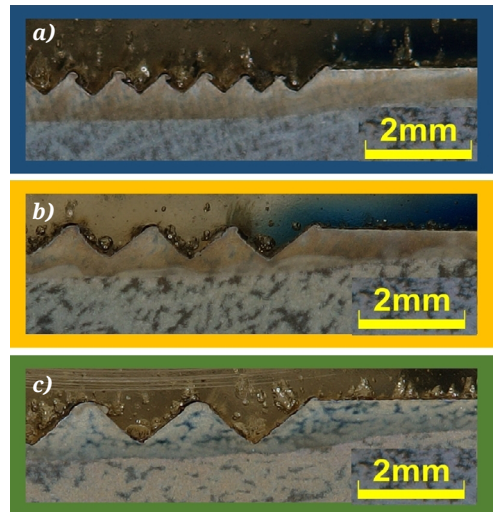


Fig. 6. Effect of laser hardening at 1600 W and 8 mm/s on grooved surfaces a) 0.25 mm grooves, sample nr. 4, b) 0.5 mm grooves, sample nr. 5, c) 0.75 mm grooves, sample nr. 6.

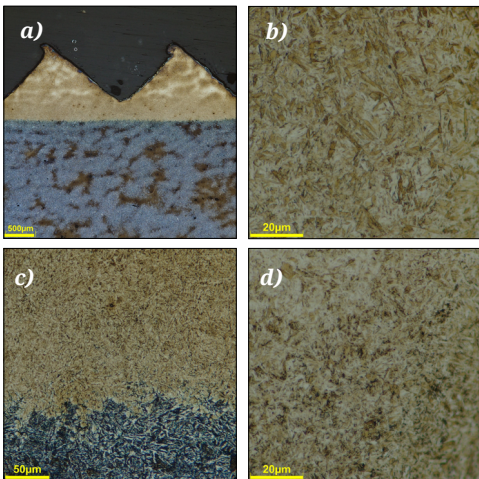


Fig. 5. Micrographs from hardened surface layer a) Microstructure of 0.75 deep milling grooved zone b) high resolutions micrographs martensitic microstructure near surface c) transition zone between surface layer and core of bar d) heat treated zone under grooves

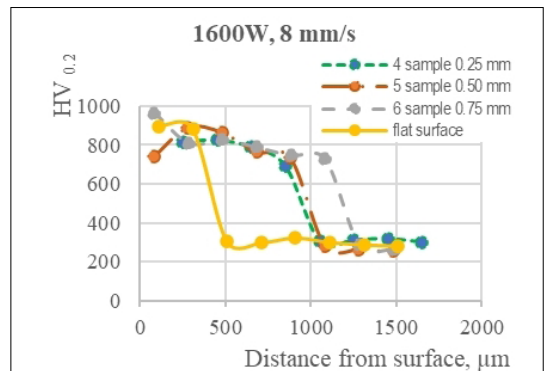


Fig. 7. Hardness versus depth curves for 200W s/mm specific laser heat input.

the laser beam power at 1200 W and reducing the scanning speed to 5 mm/s (applying 240 W s/mm specific power), the hardened layer thickness reached 500 μm even for flat surfaces. The groove design enhanced the depth of the hardened surface layer (Figure 8). Preparing the milling grooves in 45°, and hence, the 45° angel incidence of laser beam caused an increase in the thickness of the hardened layer. The effect of incidences angle modification of the laser beam on the hardened layer thickness is particularly visible on the micrograph in Figure 8.c).

At the application of 240 Ws/mm specific power, the thickness of hardened layer in case of 0.25 mm grooves did not reach 1 mm, but in case of 0.5 mm depth grooves the martensitic microstructure was still detectable at 1100 μm distance from the surface. In case of 0.75 mm deep grooves, the hardness exceeded 600 HV0.2 at a depth of 1200 μm (Figure 9).

4. Conclusions

In case of pre-hardened 42CrMo4 steel increasing the specific laser energy input during laser beam surface hardening increases the depth of hardened surface layer.

The change in the angle of incidence results in a change in the surface area of the laser beam on the material surface, which affects the power density and the energy input along the path. The angle of incidence of the laser beam at 45° increased the depth of laser hardened layer versus flat surface.

The surface hardened layers in zone of deeper grooves were deeper at the same laser power. When flat surfaces were hardened by laser beam hardening, the depth of hardening was the smallest.

The grooved surfaces formed with 0.25 mm, 0.5 mm and 0.75 mm milling depths were hardened to full depth even at 150 Ws/mm specific heat impute.

References

- [1] Bagyinszky Gy., Bitay E.: *Felületkezelés*. Erdélyi Múzeum-Egyesület, Kolozsvár, 2009. 41–45. <https://doi.org/10.36242/mtf-05>
- [2] Michał K., Jerzy M., Dominika P., Piotr W.: *Laser heat treatment of gas-nitrided layer produced on 42CrMo4 steel*. Inzynieria Materralowa, 2015. 301–305. <https://doi.org/10.15199/28.2015.5.21>
- [3] Senthil Kumar P., Jegadheesan C., Somasundaram P., Praveen Kumar S., Vivek Anand A., Ajit Pal Singh, Jeyaprakash N.: *Review on laser sur-*

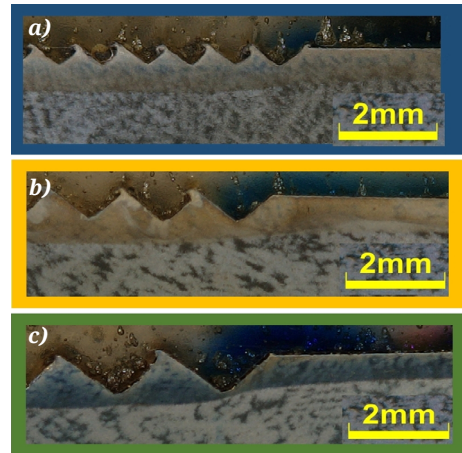


Fig. 8. Micrographs taken after heat treatment with 240 W s/mm specific laser heat input a) 0.25 mm depth grooves, sample nr. 7, b) 0.5 mm depth grooves, sample nr. 8 c) 0.75 mm depth grooves sample nr. 9.

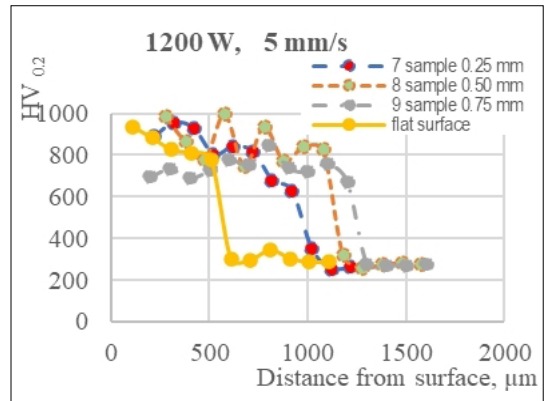


Fig. 9. Hardness plots as a function of distance from the surfaces in case of 240 W s/mm specific laser heat input.

face hardening of alloy metals. Materials Today: Proceedings, 2023. 1–5.

<https://doi.org/10.1016/j.matpr.2023.04.259>

- [4] Kádas G., Fábíán E. R.: *Komplex felületi hőkezelések hatása szerkezeti acélok tulajdonságaira*. XXVI. Nemzetközi Gépészeti Konferencia, Marosvásárhely, Románia, 2018.
- [5] Bitay E.: *Lézers felületkezelés és modellezés*. Erdélyi Múzeum-Egyesület, 2007. <https://doi.org/10.36242/mtf-04>
- [6] Buza G.: *Lézersugaras technológiák I*. Kézirat. Edutus Főiskola, Tatabánya, 2012.
- [7] <https://www.laserfocusworld.com/articles/2011/04/laser-marking-how-to-choose-the-best-laser-for-your-marking-application.html> (accessed on: 2024. 01. 25.)

- [8] Seibold G.: *Absorption technischer Oberflächen in der Lasermaterialbearbeitung*. Herbert Utz Verlag, Munich, Germany, 2006; ISBN 3831606188.
- [9] Bergström D.: *The Absorption of Laser Light by Rough Metal Surfaces*. Ph.D. Thesis. Luleå University of Technology, Luleå, Sweden, February 2008.
- [10] Kügler H.: *Effects of Short-Term Laser Beam Heating on the Absorptivity of Steel Sheets*. *Journal of Manufacturing and Materials Processing*, 3/2. (2019) 41.
<https://doi.org/10.3390/jmmp302004>
- [11] Cserjésné Sutyák Á., Szilágyiné Biró A.: *Acélok edzhetőségének becslése kémiai összetétel alapján*. *Gép*, 63/11. (2012).
- [12] Artinger I., Csikós G., Krállics Gy., Németh Á., Palotás B.: *Fémek és kerámiák technológiája*. Egyetemi jegyzet (45035). Műegyetemi Kiadó, Budapest, 1997.
- [13] MSZ EN ISO 683-2:2018 *Hőkezelhető acélok, ötvözött acélok és automataacélok. 2. rész: Ötvözött nemesíthető acélok*, 2018.
- [14] Dewi H. S., Volp J., Kaplan A. FH.: *Leaser beam absorbtion depending on the angle of incidence on groud surfaces*. *Laser in manufacturing conference, LIM*, 2019. 1–6.
- [15] MSZ EN ISO 6507-1:2024 *Fémek. Vickers-ke-ménységmérés. Mérési eljárás*, 2024.



Examination of the Weld Brazed Joints of Steel and Aluminium Thin Plates

Dániel NAGY,¹ Levente Tamás KATULA²

¹ *Budapest University of Technology and Economics, Faculty of Mechanical Engineering, Department of Materials Science and Engineering, Budapest, Hungary, dnagy.shift@gmail.com*

² *Budapest University of Technology and Economics, Faculty of Mechanical Engineering, Department of Materials Science and Engineering, Budapest, Hungary, katula.levante@gpk.bme.hu*

Abstract

In our research, overlapped thin sheets of hot-dip galvanized steel and aluminum alloy were bonded by braze welding, for which we used the CMT (Cold Metal Transfer) sub-versions of the welding manufacturer Fronius. The settings of the welding parameters were based on the smallest possible heat input and the thickness of the zinc layer. Cohesive bonds on the aluminum side and adhesive bonds on the coated steel side were subjected to metallographic test and the composition and distribution of the resulting intermetallic compounds were determined with the help of literature sources. Based on visual inspection, aesthetic and well reproducible joints were formed, but large amounts and sizes of porosities were formed on the cross-sectional grinds due to the burning of the zinc layer. We also deduced the strength characteristics of the joints from the shear-tensile tests and the fracture surfaces. The fracture of the test specimens occurred at the junction of the weld metal and the aluminum base material.

Keywords: *braze welding, CMT, mixed joint, intermetallic compound.*

1. Introduction

The appearance of aluminum and steel mixed joints was advocated by the vehicle industry after the turn of the millennium. Weight reduction and the ever-increasing resistance of structural elements to stress require solutions in which it becomes necessary to bond different metals. In the vehicle industry gluing or welding is the most often preferred. Ideally, during welding, the surface of the steel does not melt and an adhesive bond is formed with the filler material, while the aluminum forms a weld metal with the filler material due to its low melting point. Even in the solid state, steel can dissolve aluminum to a small extent, which results in the precipitation of intermetallic compounds [1]. The majority of the 6 stable (FeAl_2 , Fe_2Al_5 , FeAl_3 , FeAl , Fe_3Al) and 3 metastable (Fe_2Al_9 , Fe_2Al_7 , FeAl_6) compounds are brittle and reduce corrosion resistance. Iron has a higher diffusion factor in aluminum [2], therefore aluminum-predominant compound phases, which are brittle, are more likely to form. From a welding technical point of view, the chemical

composition of the filler material and the use of pulse process variants can also affect the appearance of brittle phases [1, 2].

Since it is not possible to prevent the formation of brittle compound phases on raw plates, a hot-dip galvanized steel plate with a pure zinc coating is most often used, which improves the corrosion properties of the seam and prevents the formation of iron-aluminum compounds by forming a bond with the aluminum, which results in a more favorable seam with low heat input. On the other hand, due to its low boiling point, it can form porosity and brittle iron-zinc compounds in the seam when burned [1, 3]. In this research, we investigated the definition, location, and shape of the intermetallic compounds appearing in the seams. The connection of thin plates is usually done by overlapping, so it is relevant to subject them to a shear-tear test and to examine the fracture surfaces. As part of the research, we looked for a correlation between the solidity characteristics and the settings of the power source.

2. Materials and experimental methods

2.1. Used materials

We welded 23 experimental joints of AlSi1MgMn and S355J2 hot-dip galvanized 0.8 mm, 1 mm and 2 mm thick plates, 100 mm long, with AlSi₅ filler material in the assembly according to [Figure 1](#). The steel plates were made with zinc coating of three different thicknesses – 24 μm (0.8 mm), 17 μm (1 mm), 123 μm (2 mm) – the effect of which on the joints is also being investigated.

For the mixed joints of aluminum and steel, non-iron-based bonding materials, such as CuSi₃, AlSi₅, AlSi₁₂ wire, are often used. The melting point of the listed welding materials must be below the melting point of the steel material and must have good wetting ability.

2.2. Welding characteristics settings

To carry out the research, we used the CMT Universal and CMT Cycle Step (CMT CS) process subversions, which were developed for the weldability of mixed joints, thin coated plates and good thermally conductive materials. These processes are characterized by low heat input, stable electric arc and thus controlled droplet separation. In a welding cycle, an electric arc is ignited by advancing the wire electrode, then a short circuit occurs and the wire is pulled back by a Push-Pull system, installed at the front of the welding torch. The sudden movement of the wire in the opposite direction separates the melted droplet and the melted electrode end falls into the seam and solidifies, and then the process is repeated. When a short circuit occurs, the system gives the instruc-



Fig. 1. Steel-aluminum overlapped plates while determining the position of the welding torch.

tion to retract the wire, so the Push-Pull control operates the forward and backward push with a time-varying frequency [\[4\]](#).

In contrast to the drop separation of short-circuit procedures this version of the procedure detects the short-circuit and prevents the high current, thereby ensuring splash-free material transfer and the formation of a large volume weld pool. CMT CS is an extension of Universal, which can create a „fish scaled” seam face at a constant speed by alternating the number of welding cycles and the pause cycles between them. It performs the number of cycles specified by the user, presented in CMT Universal, and then restarts the process after taking a pause for a given time, so the heat input is even smaller compared to CMT Universal [\[4, 5\]](#).

2.3. Metallographia and test specimens

2.3.1. Microscopy

The metallographic evaluation was performed with an Olympus PMG-3 optical microscope and a Zeiss EVO MA 10 scanning electron microscope (SEM) [\[6\]](#). In addition, energy dispersive spectroscopy (EDS) was used to determine the chemical composition of the weld [\[7\]](#).

2.3.2. Tensile test specimens

The strength of the overlapped joints was determined by testing non standard shear-tensile specimens [\[8\]](#) on a MTS 810 tensile machine. The force was introduced on non joint gaped plates, which caused eccentric tensile, shear and bend stresses in the plates. Depending on the location of the fracture, the failure may occur I.) in the heat-affected zone, II.) in the weld metal, III.) in the base material, or IV.) the seam may separate at the junction of the weld metal and the steel plate, as shown in [Figure 2](#). In the research, the tearing experiment served as a comparative study.

3. Results and their evaluation

We evaluated 18 out of 23 joints in the research. By changing the travel speed of the welding torch and the welding power, we found the speed range between 30 cm/min and 60 cm/min, at which the zinc layer burn doesn't cause an excessively porous, splattering seam. The favorable setting of the arc length correction value helped to minimize arc bending, which was caused by the better conductivity of the aluminum.

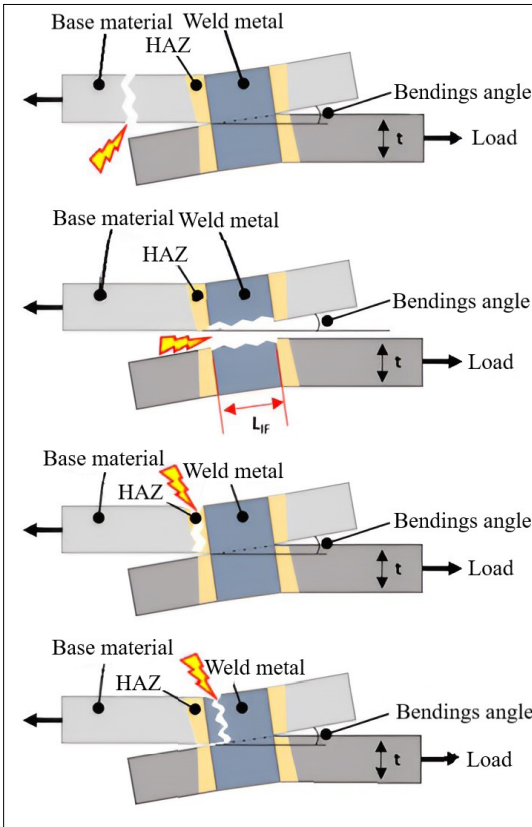


Fig. 2. Failure modes of tensile-shear test specimens in the case of lapped joints.

3.1. General weld seam characteristics

For a more in-depth review, we prepared metallographic grindings. In most of the roots, incomplete fusion occurred along the entire length of the weld (Figure 3).

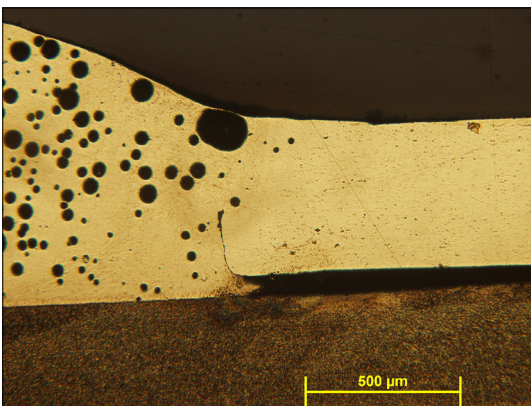


Fig. 3. Gas porosities and incomplete fusion in the weld seam cross-section.

This could have resulted from the zinc gases trying to escape towards the tightly compressed plates [9]. Due to the large number and size of porosity, none of the welds would meet the quality level D of the aluminum standard [10] because the diameter of the individual gas porosities is in many cases greater than 600 μm, and the uniformly distributed porosity percentage is greater than 2.5 % in the cross-section area.

3.2. Intermetallic compounds

In general, it can be said that the zinc layer in the weld cross-section is completely burnt or partially incorporated into the weld metal [11]. As expected, intermetallic compounds were formed when the steel and the filler material came into contact. In all cases, the compound phases arranged in layers and they are located in the center line of the seams. Their maximum width is 1.5 mm. Along the length of the seam, the compound phases appear in different spots, which may have been caused by temperature differences in the contact line of the base materials.

To identify the compound phases formed in the seams, literature research was used as a basis [2, 12]. As expected, intermetallic compounds were formed when the steel and the filler material came into contact. In all cases, the compound phases arranged in layers and they are located in the center line of the seams. Their maximum width is 1.5 mm. Along the length of the seam, the compound phases appear in different spots, which may have been caused by temperature differences in the contact line of the base materials. To identify the compound phases formed in the seams, literature research was used as a basis (Figure 4). The compound phase FeAl_3 also

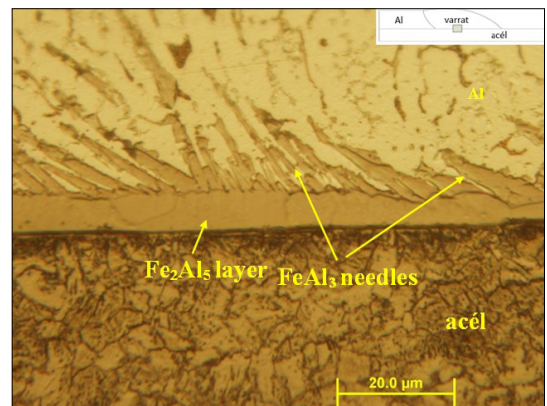


Fig. 4. Determination of intermetallic compound phases at the junction of steel and weld metal.

appears above the Fe₂Al₃ layer in the form of needles.

In the case of joints made with the CMT Universal subversion, a limit of heat input can be observed – between 0.72-0.80 kJ/cm – where the intermetallic layer thickness becomes measurable. Below this heat input, a weak oxide layer or a few μm thick phase appear at most. Continuous layers with a thickness greater than 2 μm can be found in the middle of the seams, where the heat input is the greatest. Based on research in the literature [13] intermetallic compounds have a significant effect on the strength of the bond when the thickness is over 10 μm.

3.3. Line scan chemical composition test

Line scan EDS analyses were made from the intermetallic transition zones. In the case of all welds, we examined the compounds between the filler material and steel bond in the center line of

the weld, where the presence of zinc in the weld metal can be clearly detected.

The eutectic contains an average of 8 % zinc in the weld for more than 100 μm long (Figure 5), so a part of the zinc forms a new eutectic alloy in the weld metal instead of turning into a gaseous state during welding (Figure 6) [14, 15, 16].

3.4. Tensile test

The tensile tests were performed on 80×15 mm specimens. In 90 % of the joints, the fracture occurred at the cohesive connection between the aluminum base material and the weld metal. It can be traced back to the release of the gases described earlier and the inadequate melting of the base material. Comparing the force-displacement curves of the test specimens (Figure 7), the bearing and deformation capacity of the welded plates coated with a thick layer of zinc stand out by far compared to those measured for other joints.

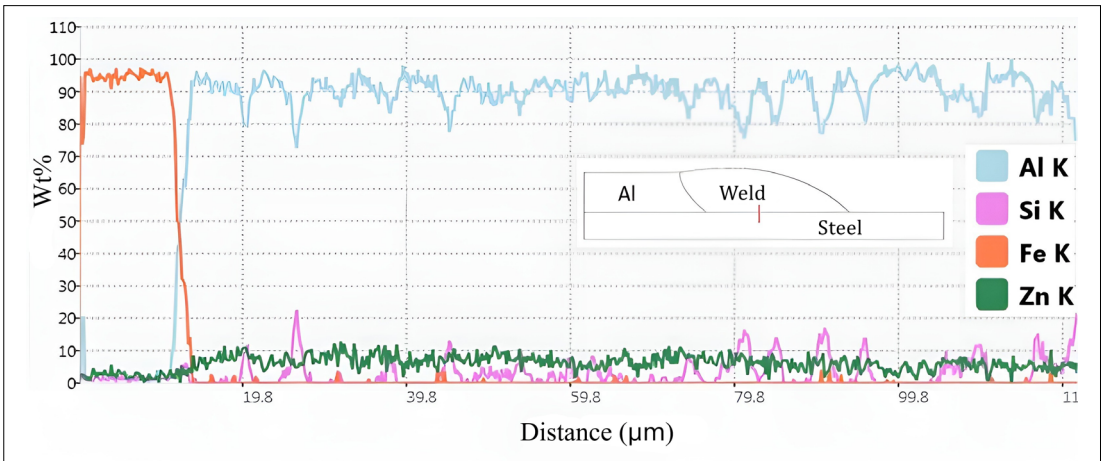


Fig. 5. EDS line scan chemical composition analyses in the line of the steel and the weld metal.

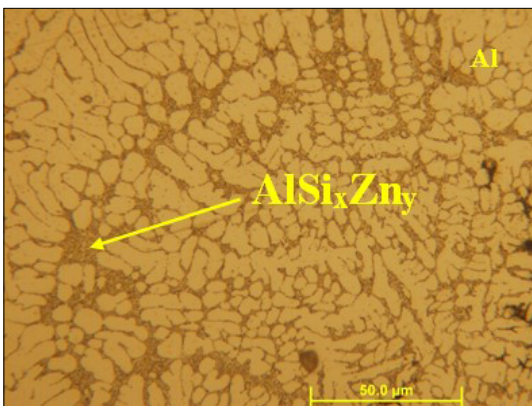


Fig. 6. Eutectic alloy in the weld metal. [16]

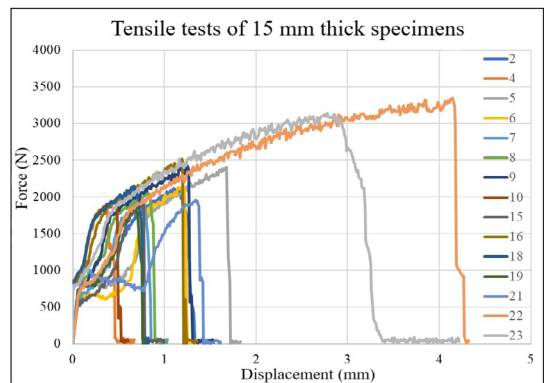


Fig. 7. Force-displacement curves recorded by tensile tests.

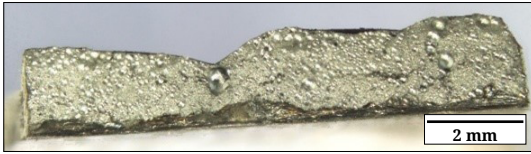


Fig. 8. Large porosities are visible on the fracture surface, which promoted the propagation of the crack.

The countless porosity visible on the fracture surfaces (**Figure 8**) played a major role in the rapid propagation of the cracks. In several test specimens, the joint cracked only up to a certain width, the complete separation occurred later in time. This was caused by the growth of porosities starting from the surface through crack propagation. The process took place with brittle fracture everywhere, before the stage of plastic deformation, the failure had already occurred.

4. Conclusions

In summary, it can be concluded that the applied welding parameters can be well reproduced with brazewelding, and appropriate seam shape and aesthetics can be formed on steel-aluminum thin plates. The large amount and size of porosities visible on the images clearly show the unfavorable effect of the zinc layer, which was not significantly reduced at any seam. The formed intermetallic compound phases could be easily identified based on the literature, and their existence was confirmed by the EDS line scan tests. Despite the fact that, in some cases, thick compound layers were also formed in the weld seams, the fracture of the joints during the tensile tests almost always occurred at the junction of the weld metal and the aluminum base material. The effect of the zinc layer thickness on the mechanical properties of mixed joint is shown by the outstanding tensile strength of the steel plate joint coated with the thickest zinc layer.

References

- [1] Kobayashi S., Yakou T.: *Control of intermetallic compound layers at interface between steel and aluminum by diffusion-treatment*. Materials Science and Engineering: A, 338/1–2. (2002) 44–53. [https://doi.org/10.1016/S0921-5093\(02\)00053-9](https://doi.org/10.1016/S0921-5093(02)00053-9)
- [2] Basak S., Das H., Pal T. K., Shome M.: *Characterization of intermetallics in aluminum to zinc coated interstitial free steel joining by pulsed MIG brazing for automotive application*. Materials Characterization, 112. (2016) 229–237. <https://doi.org/10.1016/j.matchar.2015.12.030>
- [3] Dong H., Hu W., Duan Y., Wang X., Dong C.: *Dissimilar metal joining of aluminum alloy to galvanized steel with Al–Si, Al–Cu, Al–Si–Cu and Zn–Al filler wires*. Journal of Materials Processing Technology, 212/2. (2012) 458–464. <https://doi.org/10.1016/j.jmatprotec.2011.10.009>
- [4] Somoskői G.: *A CMT eljárás elméleti alapjai és gyakorlati alkalmazási lehetőségei*. In: 25. Jubileumi Hegesztési Konferencia, Budapest, 2010.
- [5] Peng M., Liu H., Liang Y., Xu W., Zhao Y., Chen Y., Weng J., Yang J.: *CMT welding-brazing of al/steel dissimilar materials using cycle-step mode*. Journal of Materials Research and Technology, 18. (2022) 1267–1280. <https://doi.org/10.1016/j.jmrt.2022.03.043>
- [6] Havancsák K., Dankházi Z.: *Páztázó elektronmikroszkópia*. ELTE Anyagfizikai Tanszék, 2018. <http://metal.elte.hu/oktatas/alkfizlab/meresleirasok/SEM3.pdf>. (accessed on: 2022. 06. 14.)
- [7] Gaston B., Protter C.: *Energy-Dispersive X-ray Spectroscopy (EDS) Franklin & Marshall College Materials Characterization Fundamentals*, CHM 412 Collaborative Text (2019) [https://chem.libretexts.org/Courses/Franklin_and_Marshall_College/Introduction_to_Materials_Characterization__CHM_412_Collaborative_Text/Spectroscopy/Energy-Dispersive_X-ray_Spectroscopy_\(EDS\)](https://chem.libretexts.org/Courses/Franklin_and_Marshall_College/Introduction_to_Materials_Characterization__CHM_412_Collaborative_Text/Spectroscopy/Energy-Dispersive_X-ray_Spectroscopy_(EDS)) (accessed on: 2022. 06. 17.)
- [8] ASTM D638: *Standard Test Method for Tensile Properties of Plastics*, 2022.
- [9] Hoang S. M., Tashiro S., Bang H.-S., Tanaka M.: *Numerical analysis of the effect of heat loss by zinc evaporation on aluminum alloy to hot-dip galvanized steel joints by electrode negative polarity ratio varied AC pulse gas metal arc welding*. Journal of Manufacturing Processes, 69. (2021) 671–683. <https://doi.org/10.1016/j.jmapro.2021.08.019>
- [10] MSZ EN ISO10042: *Hegesztés. Alumínium és ötvözetek ivhegesztéssel készített kötése. Az eltérések minőségi szintjei*, 2018.
- [11] Yang J., Hu A., Li Y., Zhang P., Saha D. C., Yu Z.: *Heat input, intermetallic compounds and mechanical properties of Al/steel cold metal transfer joints*. Journal of Materials Processing Technology, 9/3. (2019) 40–46. <https://doi.org/10.1016/j.jmatprotec.2019.05.004>
- [12] Zhang G., Chen M. J., Huang J., Yang F.: *Analysis and modeling of the growth of intermetallic compounds in aluminum–steel joints*. Royal Society of Chemistry, 7/60. (2017) 37797–37805. <https://doi.org/10.1039/C7RA06354G>
- [13] Zhang W., Sun D., Han L., Gao W., Qiu X.: *Characterization of Intermetallic Compounds in Dissimilar Material Resistance Spot Welded Joint of High Strength Steel and Aluminum Alloy*. ISIJ International, 51/11. (2011) 1870–1877. <https://doi.org/10.2355/isijinternational.51.1870>

- [14] Kakitani R., Konno C., Garcia A. Cheung N.: *The Effects of Solidification Cooling and Growth Rates on Microstructure and Hardness of Supersaturated Al-7%Si-x%Zn Alloys*. Journal of Materials Engineering and Performance, 31. (2022) 1956–1970.
<https://doi.org/10.1007/s11665-021-06341-8>
- [15] Ishaq M., Basariya R., Mukhopadhyay N. K.: *Structural and Mechanical Behaviour of Al-Fe Intermetallics*. IntechOpen, Irán, 2018. 226.
<https://doi.org/10.5772/intechopen.73944>
- [16] Septimio R., Silva C. A. P., Costa T. A., Garcia A., Cheung N.: *Hypereutectic Zn–Al Alloys: Microstructural Development under Unsteady-State Solidification Conditions, Eutectic Coupled Zone and Hardness*. Metals, 12/7. (2022) 1076.
<https://doi.org/10.3390/met12071076>



Laser Engraving on a CNC Milling Machine

Viktor Gergely RÁCZI,¹ Balázs MIKÓ²

¹ Óbuda University, Doctoral School on Materials Sciences and Technologies, Budapest, Hungary, raczi.viktor@bgk.uni-obuda.hu

² Óbuda University, Bánki Donát Faculty of Mechanical and Safety Engineering, Institute of Mechanical Engineering and Technology, Budapest, Hungary, miko.balazs@bgk.uni-obuda.hu

Abstract

This article details how a commercially available diode laser (VoidMicro LD4070HF Pro) can be integrated into a conventional 3-axis CNC milling machine (HAAS Mini Mill Edu). Thanks to this development, the CNC milling machine is now able to perform a new machining process. The laser module has a major impact on the development of the secondary time, in addition to the rapid execution of engraving operations, i.e. by reducing the production lead time. During the production of a part, the marking of the product, such as QR code and barcode, is also carried out on a single machine tool, thus reducing the production cost. An additional benefit of integrating a laser engraver is that the CNC milling machine can also be used for laser cutting thin plastic and wood panels.

Keywords: *Laser diode, CNC milling machine, Engraving, Arduino.*

1. Introduction

The aim of the research is to make the 3-axis CNC milling machine (HAAS Mini Mill Edu) at the Bánki Donát Faculty of Mechanical and Safety Engineering of Óbuda University suitable for a new machining process. By integrating a commercially available laser engraving head (LD4070HF Pro), laser engraving operations are also carried out on the CNC milling machine.

Therefore, an additional machining operation can be carried out on the CNC milling machine, so that marking or engraving tasks can be fulfilled on a single machine, thus saving significant time and costs.

1.1. The justification for laser engraving today

Today, the dynamic evolution of the competitive market is forcing machining companies to make better use of technical innovations. In the case of series production, the emphasis is on shortening the primary and secondary machine times (62 % of production costs [1]) and on the economical use of production tools, which enables manufacturing companies to optimise their production costs. Reduction of manufacturing lead, and lead times

can be achieved by using new machining processes (e.g. trochoidal cutting (TPC), high-speed cutting (HSC), high-performance cutting (HPC) [1]) and new generation tools (multi-tasking tools (MTC)). In addition, we can reduce downtime and costs by trying to manufacture products using as few machining and production support machines as possible [2].

1.2. Laser marking

In classical engraving, a small amount of material is cut from the surface of the workpiece at different depths, which creates the desired pattern, image, inscription or number sequence readable on the workpiece. Nowadays, almost all products are provided with an identification number, barcode or QR code (QR = quick response) to identify the product, so marking equipment, and marking lasers, are now used for these markings to increase productivity. Laser marking is most commonly used for metal and plastic parts [3].

1.2.1. Laser marking of metal parts

Three types of marking processes are used by industry for metal parts [3]. One is engraving, where the laser beam power is so high that the material melts and partially vaporises (evapo-

rates) during machining. This results in indentations of 10–50 μm in the workpiece [4]. In the case of deep engraving, laser engraving must be repeated several times at different depths to avoid distortion. With good alignment parameters, the cross-sectional shape of the engraving is U-shaped. The readability of the engraving is due to the fact that after the process the engraved surface is reflected differently by the light, thus making the laser engraving pattern readable. The process requires the usage of a high-power laser ($P > 50\text{ W}$), such as a pulsed mode laser, Nd: YAG (neodymium-doped yttrium aluminium garnet) or Nd: YVO₄ (neodymium-doped yttrium orthovanadate). The focal spot of the laser beam is placed on the surface of the workpiece. This process is most commonly used in tool and die manufacturing or for engraving vehicle identification numbers [3, 4].

The other metal marking method is heat treatment and colouring. The process changes the structure of the material so that melting does not occur. The laser beam heats the material of the workpiece to a temperature below the melting point, which can change the fabric structure of the material and form a corrosion product on the surface with air components. The surface of the workpiece will then appear in different colours. In contrast to laser engraving, this process can be performed with a much lower energy pulse, allowing the use of machines with continuous wave lasers. The lasers used for laser colouring are continuous or pulsed transistors, pulsed Nd: YAG or Nd: YVO₄ lasers. In laser annealing or colouring, the focal length must be set above the surface of the workpiece, so that the laser beam only applies a large amount of heat to the surface, but does not melt it. This marking process is most often used by industry to mark medical devices, as it avoids the formation of indentations that can harbour bacteria. It is also widely used for marking measuring instruments (e.g. calipers) and tools. The disadvantage of this process compared to laser engraving is the longer machining time, so engraving is preferred by industry for mass production [3].

The third metal marking method is laser marking using a special paste. The main advantage of this method is that it can be used with low-power lasers ($P < 50\text{ W}$) For this reason, „laser paste” marking (available in spray, tape or diluted form) is the most common method of marking with CO₂ lasers. This procedure is only applicable to uncoated metals [3].

1.2.2. Laser marking of plastic parts

In the case of laser marking plastics, four laser marking processes are distinguished [5]. One of the marking process produces bubbles when heat is applied to the surface, and is therefore called foaming marking. During the process, the surface and surface roughness of the workpiece is changed, which makes the marking on the surface of the workpiece visible [3, 5].

The other method is thermal colouring, also known as marking of metallic workpieces. In this process, no material is removed from the surface of the workpiece, only the tissue structure of the material particles on the surface of the workpiece are altered by laser radiation, which can be either thermal or photochemical. In the case of thermal dyeing of plastics, it is also possible to perform thermal dyeing using a much lower power laser ($P < 50\text{ W}$) Both processes can be performed using pulsed lasers, Nd: YAG, Nd: YVO₄, CO₂ solid-state lasers and diode lasers [3, 6].

The third method is the engraving process presented for metallic components, while the fourth marking variant is coating removal by laser beam [5].

2. Methods

In the first part of the design, we identified the main tools to be used. The main criteria for the choice of the laser module were the price/performance ratio and ease of availability. In the case of a CNC milling machine, the main criteria for choosing the machine were the machine availability and the possibility of breaking the machine enclosure. In connection with control electronics, we also sought to ensure reliability and a favourable cost price, while ease of programming was also taken into account.

2.1. LD4070HF Pro engraving head

For the engraving head used, a laser module, LD4070HF Pro, manufactured by VoidMicro and widely used in hobby engraving machines, was chosen (Figure 1). The laser module produces a beam at 450 nm wavelength and a constant focal length (15 mm from the focusing lens). The input power is 40 W and the output power is 7.5 W. The system operates at 12 V and its power is controlled by a pulse width modulation (PWM) signal. The engraving head is not only capable of engraving due to its power, but also of cutting wooden sheets up to 3–5 mm thick and plastic sheets up to 3 mm thick [7].



Fig. 1. LD4070HF Pro engraving head real and virtual appearance.



Fig. 2. Haas Mini Mill EDU

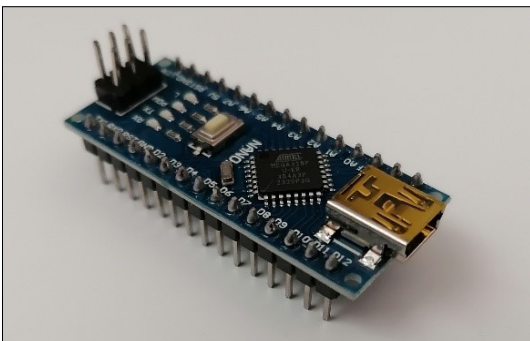


Fig. 3. Arduino Nano microcontroller.

2.2. Haas Mini Mill EDU CNC milling machine

The laser module application was designed for the Haas Mini Mill EDU CNC milling machine (Figure 2).

The CNC milling machine has a maximum speed of 4000 rpm and a maximum power of 5.6 kW. The machine tool has a working area of 406×305×254 mm. But does not have cooling system and automatic tool changer [8].

During the design phase of the project, the objectives of the project were defined taking into account the characteristics of the machine (CT 40 main spindle end [8], lack of cooling and tool change system).

2.3. Arduino Nano

The PWM (pulse-width modulation) signals used to control the laser module are controlled by an Arduino microcontroller in the case of custom digital controllers.

Arduino is a generic term that includes both a simple electronic circuit (hardware) and an open-source platform (software) based on a software development environment. The hardware consists of an electronic circuit built around an Atmel AVR microcontroller, while the software part is a C-based program called Arduino IDE, using the C++ programming language. Arduino can be used to create interactive objects, as it can receive and send digital signals and also process analogue signals. It can even control motors, sensors, lights, etc. The program, written with the Arduino IDE software, can be programmed to the microcontroller via USB after being translated into the appropriate language. The program consists of two main parts. The setup section contains the basic settings, while the loop section contains the actual operations to be performed. Consequently, the setup part runs only once, while the execution of instructions in the loop part is repeated in an infinite loop [9].

To save space, the laser module was controlled using one of the smallest commercially available Arduino Nano microcontrollers (Figure 3).

3. Building and controlling a custom engraving head

The design phase started with the reverse engineering of the engraving laser elements using Catia P3 V5R21 CAx software.

The factory laser module was built up of 30 parts, including screws, spacers and the control

circuit board in addition to the main building blocks.

After reverse engineering, the mounting options in the main spindle were investigated. In the first concept, the original fan was replaced by two radial turbo fans, which would have been placed on the side of the laser module. As a consequence, the original length of 113.7 mm is shortened, making the laser module more robust and the cooling more intensive. The disadvantage of this concept is that the radial fans could be damaged during manual tool change, so we decided to use an axial fan instead of a radial fan based on the second concept. To further reduce the length size, it was considered appropriate to relocate the laser module controller.

During the reverse engineering, a mounting error was found in the original engraver's heat sink (hole enlargement with a hand tool). A mismatch of 0,3 mm was measured between the diameter of the laser diode and the bore of the heat sink. The laser diode was fixed with a M3×8 mm hexagon socket head screw (DIN 916 standard), which pressed the laser diode radially against the wall of the heat sink bore (Figure 4, area marked with yellow). Consequently, the significant heat generated by the laser diode was transferred along an edge to the heat sink, making the cooling efficiency questionable at a maximum laser power of 40 W. Due to the aforementioned shortcomings, we decided to design and manufacture a custom cooling fin and its custom mounting elements instead of the original laser diode housing.

3.1. Individual heat sink

In addition to maximising the cooling of the laser diode, the main considerations in the design of the custom heatsink were reducing its length, ensuring an adequate power supply, avoiding contamination of the focusing lens and measuring the temperature of the laser diode. The housing elements were made of AW-6082 aluminium. The chosen material has good strength, good machinability and good thermal conductivity.

The cooling intensity of the laser engraver was increased in several ways. In addition to creating fins in the cooling component, heat dissipation was increased by circulating compressed air in 14 holes around the laser diode sheath. At the laser diode location, a $\varnothing 20.7$ mm H7 hole was drilled to ensure a seal between the sheath surfaces. To increase heat transfer, a heat-conducting paste was applied between the heat sink and the diode laser (Figure 5).

To measure the current temperature of the diode laser, we use an NTC 10K thermometer, whose signals are processed by the Arduino Nano. The measuring range of the thermometer is -30 – 120 °C, while the accuracy is between 4 – 50 °C $\pm 2\%$. The measuring device can be integrated into DC 2.2–12 V electrical systems.

The electrical connection is solved by a 6-pin Pogo pin connector. To avoid damage to the Pogo pin contacts, 2 to 2 contacts are used to connect the diode laser to the controller. Due to the limited space availability, we designed a unique pin



Fig. 4. Factory Cooling System Failure of the Laser Module.



Fig. 5. Top view of the heat sink.

board for the Pogo pin connectors. The plastic element of the custom engraving enclosure was by made using a 3D printer (Creality Ender 3 v2) from PLA (Polylactic acid) material.

Since the CNC milling machine has no cooling system either outside or inside the main spindle, a compressed air-cooling system had to be built as part of the project. The compressed air is supplied to the cooling fins through a $\varnothing 6$ mm pipe coil (Aventics TU1-S-PUR 006-0105-NT-100) via a pneumatic connector (Aventics QR1-AAN G014-DA06). The compressed air, in addition to cooling the heat sink, prevents contamination (soot build-up) of the focusing lens by directing the compressed air out of the laser diode housing in front of the lens, parallel to the laser beam.

The length of the case we designed is 85 mm, 25 % smaller than the original 113,7 mm. The new laser diode housing can be easily fixed by using industry-standard tool clamping devices (e.g. ER cartridge tool clamps). The symmetry axis of the custom heatsink can be adjusted within a range of 1 mm using 3 cage screws positioned at 120° , allowing the heatsink to be made uniaxial to the main spindle.

The final construction is made up of 62 elements, including screws, electrical connectors and gaskets in addition to the main components **Figure 6** illustrates a virtual model of the custom heat sink and the fabricated and assembled laser diode housing.



Fig. 6. Virtual and real appearance of the assembled laser diode house.

3.2. Housing of the power supply module

The electronic systems operate on 12 V and 5 V supply voltage. The electrical system of the CNC milling machine could not be used due to the warranty contract, so the power supplies for the electronic systems were built using the 115 V power socket on the side of the CNC milling machine. Since the Arduino control electronics system is sensitive to small voltage fluctuations, we used an AC/DC switching power supply module (PXX-2412DC-12V) to generate the power supply voltage for our electronics systems.

The power supply module was used to convert the 115 V (AC) voltage coming out of the power socket of the CNC milling machine to 12 V (DC) voltage. The resulting voltage is now suitable for powering the electronics of the engraving head, but further transformation is required to power the Arduino electronics. The generation of the voltage for the Arduino system is detailed in section 3.4.

For the electronics enclosure, we used a computer power supply enclosure. The cooling fan in the original power supply was used to cool the electronics. To ensure safe operation, we can interrupt the incoming 115 V voltage using a two-position toggle switch (ST 1/BK (MRS-1)), thus completely de-energizing the electronics we want to control. During machining, it is not possible to access the rocker switch due to the CNC milling machine door housing, so thanks to the CNC machine emergency stop switch housing, the 12 V generated by the power supply module can be interrupted by installing an Eaton m22-k01 opening contact. This ensured that the use of the emergency stop button not only locked the movements of the CNC machine, but also switched off the laser module and the electronics controlling the laser module. In addition, a digital voltmeter was installed in the power supply circuit to monitor the 12 V supply. To measure the laser diode power, we used an ACS712 5A Hall-element current sensor module, also mounted inside the power supply module housing (**Figure 7**).

3.3. Housing of the laser diode electronics

We designed a separate housing for the electronic control unit of the LD4070HF Pro engraving head, which we wanted to place on the side of the main spindle of the CNC milling machine. When designing the housing of the laser module's electrical circuit controller, we took into account that the engraving head manufacturer distributes

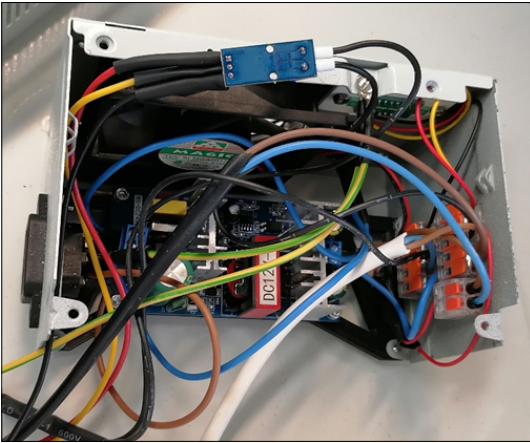


Fig. 7. Housing of the assembled power supply module.

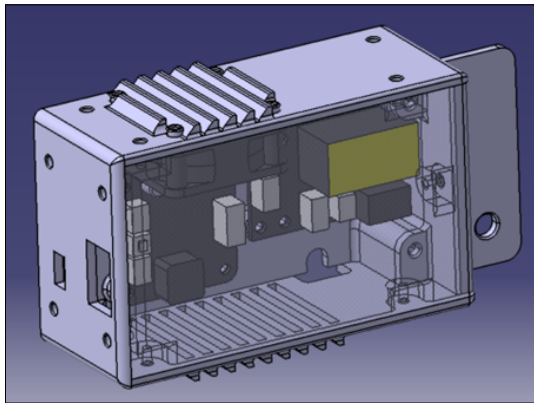


Fig. 8. Virtual 3D drawing of a laser control circuit housing.



Fig. 9. The control housing of the assembled laser engraver.

an additional electronics interface and adapter board, which is used to provide several electrical connections to supply the laser module's electrical and control power. By using the aforementioned hub board, we decided to connect the electrical wiring through the pigtail on the hub for easy installation. In addition, the design of the enclosure took into account the need to cool the laser module's control electronics to avoid overheating at high power consumption. To this end, we can ensure cooling of the electronics by using the cooling fan in the original engraving head, so that a control built into the control electronics turns on the fan when the power consumption of the laser head reaches 3 % of the maximum power. **Figure 8** illustrates the virtual elements of the laser control electronics housing.

The housing enclosure elements were printed using a 3D printer using PLA in RAL 9016 colour code (**Figure 9**).

3.4. Housing of the controller electronics

Using the Arduino Nano, as described in chapter 2.3, it was possible to control not only the engraving head, but also other control electronics simultaneously. The designed Arduino program will be presented in chapter 4.1, in this chapter we will only detail the electronics to be incorporated and the housing designed to mount them.

For ease of assembly, a standardized terminal adapter board has been added to the Arduino Nano slot board. A voltage of 12 V is used by the LEDs of the pushbuttons (V19-11R-12G/R) in the custom enclosure. The operating voltage of the Arduino Nano is 5 V, so to transform the 12 V supply voltage, we used a STDN-3A24-ADJ factory number 3 A adjustable step-down DC-DC switching power supply module. To enable the Arduino to control the 12 V LEDs in the pushbuttons, a 4-channel bi-directional logic level-shift driver LS-BIDI-4 was used, which causes a 5 V signal connected to any of the 4 inputs of the circuit to produce a 12 V output signal.

When designing the engraving head control, we took into consideration the CNC milling machine's operating conditions. The push buttons „cycle start” (Eaton 216512 M22-D-G-X1/K10) and „feed hole” (Eaton 216510 M22-D-R-X0/K01) on the CNC milling machine not only allow to control of the start and stop of the active machining program on the CNC milling machine but also influence the operating status of the laser head by means of the Eaton 216376 M22-K10 contact elements mounted in the push buttons.

To generate and control the PWM signal, a 100 k Ω analogue 270° rotating potentiometer was used, so we could adjust the laser diode power during machining.

In addition to the electronics listed above, the electronics (pull-down resistor) for the NTC 10K type thermometer described in section 3.1 were also incorporated here. In order to facilitate the control of the laser diode, a 1602 LCD (Liquid Crystal Display) and associated control electronics were used to display data during the operation of the laser diode.

The design of the custom enclosure was not only based on the size of the electronic components, but also on aspects of ergonomics and aesthetics. When designing the enclosure components, we had to take into consideration the manufacturing conditions, so we had to keep in mind the range of motion (x-y direction) of the 3D printer used (Creality Ender 3 v2). In addition, the enclosure has been designed with a modular approach to allow for future expansion. The enclosure we have designed is illustrated in [Figure 10](#).

For the cladding, we also used 3D printing to create a large part of the elements we designed, using PLA in RAL 9016. The front panel was laser-cut from a 2 mm thick stainless-steel sheet (X5CrNi18-10) for aesthetic appearance ([Figure 11](#)).

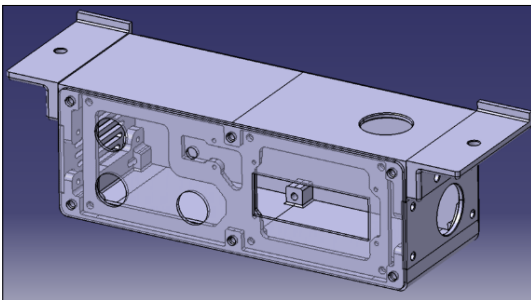


Fig. 10. Enclosure of the electronics for the engraving head controls.



Fig. 11. Enclosures for laser head control electronics.

4. Operating a diode laser using a CNC milling machine controller

The operation of the laser engraver was solved by 5 M-code controlled relays (I/O PCB output) on the Haas Mini Mill EDU controller electronics. The relays can operate in two ways. In the first case, by using the appropriate M-code, the contacts of the relays, which are isolated from the CNC milling machine circuits, can control up to 3 A current at 120 V AC. The relays are of SPDT (Single Pole Doble Throw) design, allowing one relay to control up to two devices simultaneously. In the other mode of operation, the relay can be put into operation by calling another M-code command, which operates until the controlled electronics sends an M-fin signal to the CNC milling machine controller, which switches the relay position to the home position [\[10\]](#).

4.1. The driver program running on the Arduino

After supplying the Arduino Nano's input with 5 V supply voltage (STDN-3A24-ADJ), the program in the Arduino's Flash memory is run continuously. The Arduino IDE program mentioned in section 2.3 was used to create the program to control the electronics. During the creation of the program, we decided that we wanted to operate the engraving head in two different ways, so we designed and built the electrical systems accordingly.

Once the Arduino's system is powered on, the setup part of the program is run and then the „Test” mode in the loop part of the program is automatically started. In the test mode, we can manually operate the engraving head by pressing the V19-11R-12G (green LED) type push button connected to the digital leg 2 (input and output) of the Arduino. The laser module operates at the 10 % PWM signal level set in the program until the push button is pressed. This allows the laser module's operability to be tested, and also provides a visual indication of the exact position of the main spindle centre on the workpiece surface (a useful feature in case of orientation). In addition to the continuous illumination of the green LED mounted on the push button, the LCD display is also used to clearly inform the operator of the status of the control cycle ([Figure 11](#)).

Another mode in the loop part of the program running on Arduino is the Cycle mode. In Cycle mode, the Haas controller can control the laser module after several conditions are met. The cycle mode can be entered by pressing the pushbut-

ton that remains in the position marked V19-11R-12R-S (red LED), which is connected to the digital leg 3 of the Arduino. The program then continuously checks whether the Arduino's digital leg 7 is receiving a signal from the relay M21, one of the relays that can be operated with code M as described in Chapter 4. In addition, by pressing the pushbuttons for the CNC milling machine's cycle start and feed hole (Eaton 216376 contacts marked M22-K10), the laser head can be turned on and off while the program is running on the CNC milling machine. Therefore, pressing the „feed hole” button will also turn the laser engraving head off when the CNC milling machine is paused, while pressing the „cycle start” button will resume the CNC milling machine program and turn the laser head back on. To indicate the cycle mode, the LED light of the pushbutton marked V19-11R-12R-S is lit red and the LCD display shows that the Arduino is currently in Cycle mode.

In its current state, the laser power (PWM signal magnitude) can only be controlled manually using the 100 k Ω analog 270° rotating potentiometer described in section 3.4. The middle output of the potentiometer is connected to the A0 leg of the Arduino (analog input 0), so I proportional the amount of resistance that can be influenced by the potentiometer to the value of the PWM signal level.

The effect of running the CNC program is to display the value of the potentiometer position in percentage on the LCD display, and in addition the power value calculated from the current value measured by the ACS712 5A Hall-element current sensor module described in section 3.2, the temperature measured by the NTC 10K thermometer described in section 3.1 is also displayed. This allows us to check the power value recorded by the laser module during machining and the magnitude of the thermal expansion due to the loss during laser diode operation.

While writing the Arduino program, we checked the correctness of the program parts in virtual space using Autodesk Tinkercad software. The circuit design module of the Tinkercad software can control the circuits assembled in virtual space, making it much easier to create a program running on the Arduino Nano, since in reality an electrical fault (for example: a short circuit) can cause fatal damage on the Arduino circuit. By using simplified virtual copies of the switches, resistors and other electronic components used in real life, we were able to design the wiring locations for the control electronics. In addition, when run-

ning the controller program, the Tinkercad program also visually displays any errors that may occur due to program errors (for example: LED malfunction).

After the control program was written in the Arduino IDE software and verified in the Tinkercad software to run without errors, we loaded the control program onto the Arduino Nano microprocessor we used. After some minor modifications (connecting the pull-down resistors), the control program worked perfectly.

Using Catia P3 V5R21 CAx software, we created an engraving etching cycle. After postprocessing, the on and off commands were replaced by M codes to control the I/O PCB output (relay). The test program run was executed without errors (Figure 12).

5. How to operate the laser safely

When using laser light, the operator's skin and eyes must be protected. Direct exposure to laser light can cause serious injury to the skin or eyes. However, even in the case of scattered (reflected) laser light, skin or eye injuries must be prevented. During the design of the project, it was determined that the enclosures of the CNC milling machine would prevent the skin from being damaged by scattered laser light. To protect the human eyes, protective goggles were required because the laser diode used is Class 4 according to IEC 60825. The required safety glasses have the property of being able to filter light from 190 nm to 540 nm with an optical density (OD) value of 5.



Fig. 12. Laser engraving made by the test program.

6. Conclusions

This article describes in detail how to integrate a diode laser in a commercially available laser engraving head (LD4070HF Pro) into an industrial CNC milling machine.

A cornerstone of our development project was to reduce the length of the original LD4070HF Pro laser engraving head to 113,7 mm. In the design, we thus sought to reduce the length dimension, so that the total length of the cooling fins and associated components of the laser engraving module we designed is 85 mm, which is 25 % less than the length of the original laser module.

In order to increase the cooling intensity of the diode laser, we have designed a custom heat sink. The cooling of the laser module was provided in several ways. A $\varnothing 20.7$ mm H7 mating hole in the heat sink provides a temporary fit for the diode laser. A significant part of the heat generated during the operation of the laser diode is dissipated by compressed air flowing through 14 holes in the individual heat sink fins. The compressed air exiting the heat sink is forced to the focusing lens of the diode laser to prevent soot deposition on the lens.

This article describes in detail the electronic systems we have designed to operate the laser module and the specific enclosures we have designed for them.

It will also be shown how to operate the laser engraving head using the CNC milling machine controller. The laser engraving head we have designed (Fig. 13) and its associated accessories are

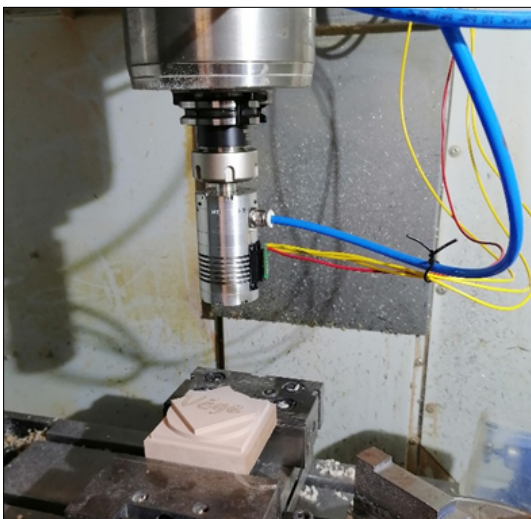


Fig. 13. Laser engraver in the main spindle.

capable of measuring and displaying the power drawn by the laser diode and the current temperature of the diode laser during machining.

The material cost of the project, which includes the electronics, wiring, fasteners, raw material for the cooling housing elements and the diode laser, amounted to 320 EUR.

References

- [1] Perfor company's website: Szerszámköltség és gazdaságos forgácsolás. <https://perfor.hu/szerszamlkoltseg-gazdasagos-forgacsolas> (accessed on: 2024. 03 19.)
- [2] Hoffmann GmbH: *Forgácsolási kézikönyv*. Hoffmann Gruppe, München, 2016. 141–161.
- [3] Ábrahám Gy., Lőrincz E., Antal Á., Tamás P.: *Lézer technika* (jegyzet). Budapesti Műszaki Egyetem, Budapest, 2015. ISBN 978-963-313-203-6
- [4] Trumpf company's website: Mi a lézergravírozás? https://www.trumpf.com/hu_HU/megoldasok/alkalmazasok/lezeres-jeloleles/lezergravirozas (letöltve: 2024. március 5.)
- [5] Kovács I.: *Lézeres jelölés* (szakdolgozat). OE-BGK, Budapest, 2017. 6–9.
- [6] Dobránszky J., Bitay E.: *Polimerek lézersugaras jelölhetősége*. XVII. Műszaki Tudományos Ülésszak, Kolozsvár, 2016. 71–78. <https://doi.org/10.33895/mtk-2017.06.07>
- [7] LD4070HF Pro laser engraving head manufacturer's website: http://voidmicro.com/Products/Laser/LD4070HF_Pro-en.html (accessed on: 2024. 03 10.)
- [8] Haas Automation cég weboldala: Haas Mini Mill EDU <https://www.haascnc.com/hu/machines/vertical-mills/mini-mills/models/minimill-edu.html> (accessed on: 2024. 03 10.)
- [9] Starduino: Arduino website for beginners: <https://starduino.hu> (laccessed on: 2024. 03. 10.)
- [10] Haas Automation company's website: Robot integrációs támogatása – NGC <https://www.haascnc.com/service/troubleshooting-and-how-to/reference-documents/robot-integration-aid---ngc.html> (accessed on: 2024. 03. 10.)



Optimization of Ultrasonic Welding of Polypropylene Sheets

Márton SCHRAMKÓ,¹ Róbert Gábor STADLER,¹ Péter PINKE,² Tünde Anna KOVÁCS²

¹ Doctoral School on Materials Sciences and Technologies, Óbuda University, Budapest, Hungary, schramko.marton@bgk.uni-obuda.hu, stadler.robert@bgk.uni-obuda.hu

² Bánki Donát Faculty of Mechanical and Safety Engineering, Óbuda University, Budapest, Hungary, pinke.peter@bgk.uni-obuda.hu, kovacs.tunde@bgk.uni-obuda.hu

Abstract

Nowadays, polymers have grown into a leading group of materials. Accordingly, many technical polymers are used in industry. As the ending knee absorption increases, the binding design is also being studied continuously. In addition to mechanical and glued joints, different welding processes stand out, such as laser welding, stirrer friction welding, and ultrasound welding. The research was carried out on polypropylene, the plastic called PP. The aim of the study is to examine the ultrasonic welding of polypropylene sheets. During welding processes, we examine the effect of parameters such as welding time, amplitude and main load on the strength of the welding seam. Based on the test results, it was possible to create high-quality joints. The highest seam strengths were obtained with a welding time of 1.2 s and an amplitude of 55 μm . The effect of the main load on the strength of the seams was minimal.

Keywords: *ultrasonic welding, polypropylene, PP, welding strength.*

1. Introduction

Plastics have emerged as a dominant material group in recent decades, making it challenging to find an industry untouched by their application. Alongside their widespread distribution, the development of high-quality, economical, and efficient bonding technologies for plastics has become essential. Among established bonding techniques, adhesive bonding and welding are particularly prominent. Both methods remain significant areas of research, with a continuous stream of publications addressing advancements in these fields. In adhesive bonding, investigations frequently emphasize the impact of various surface treatment methods and the application of different adhesive materials [1, 2].

In the field of plastic welding, notable techniques include laser welding [3], friction stir welding [4], and ultrasonic welding. Ultrasonic welding possesses several advantageous properties—such as high joint quality, speed, cost-effectiveness, and suitability for automation—that facilitate its widespread industrial application for both metals and plastics (e.g., in the automotive industry) [5, 6].

The broad industrial adoption of ultrasonic welding provides a robust foundation for ongoing research and publications aimed at advancing and optimizing this technology. Key research areas include studies on welding various material combinations (e.g., copper and aluminium [7], metal-polymer interfaces [8]), welding plastic matrix composites [9], and optimizing welding parameters [10]. Additionally, the widespread use of polymeric materials and ultrasonic welding technology has led to a marked increase in studies specifically focused on the ultrasonic welding of plastics.

Kiss and his team [9] conducted an investigation into the ultrasonic welding of polypropylene matrix composite plates (APPC). The variable modified during the experiments was the welding time, which ranged from 0.1 to 1.0 seconds. Following the welding process, the strength of the seams was assessed. Based on the results obtained, it was determined that the bond strength of the raw material was effectively achieved.

Kawasaki and his team [10] investigated the temperature distribution during the ultrasonic welding of a carbon fiber-reinforced polypro-

pylene matrix composite (CF/PP). In their experiments, the amplitude of the sonotrode and the welding time were varied at three levels. In addition to measuring the temperature and its distribution, single-shear tests were conducted on the welded joints. The results confirmed that the amplitude of the sonotrode significantly influences both the temperature distribution during welding and the quality of the joint, thereby affecting the mode of failure.

Raza and his team [11] investigated the ultrasonic welding of polypropylene (PP) and acrylonitrile butadiene styrene (ABS) sheets using a Taguchi experimental design. During the experiments, in addition to the two different thermoplastic materials, two types of energy control geometries (triangular and semicircular) were varied, along with welding time, amplitude, and pressure. After the welding process, the tensile strength of the seams was evaluated using a shear test. Additionally, welding energy was considered as a parameter. Based on the test results, both PP and ABS exhibited similar trends concerning the various parameters, and in both cases, the triangular energy-opening geometry produced superior bond quality.

Rajput and his team [12] investigated the effects of welding variables (e.g., welding time, holding time, amplitude, etc.) during the ultrasonic welding of H110MA polypropylene. The authors varied these parameters at three levels each. The Taguchi method was employed to plan the measurement points, while analysis of variance (ANOVA) was utilized for evaluation. The primary output parameter tested was the separation resistance. Based on their measurements, the authors demonstrated that amplitude had the most significant effect on detachment resistance.

As demonstrated in the aforementioned publications, the ultrasonic welding of polypropylene (PP) materials is a prevalent research topic. It is noteworthy that PP is the second most widely produced polymer and is utilized extensively in leading industries, including the automotive and medical sectors [13].

The purpose of this study is to investigate the ultrasonic welding of PP material, optimize the input parameters, and determine their effect on the strength of the weld seam.

2. Material and methodology

During our experiments, 4 mm thick DOCAPRÉN-H polypropylene plates were welded together. The



Fig. 1. The welding machine used during the experiments

welding was conducted using a BRANSON ultrasonic welding machine. Each plate measured 10 mm in width, and the overlap was also 10 mm; consequently, the area of the point joint was 100 mm², with a length of 70 mm (see Figure 1).

Based on the literature review, we conducted two series of experiments. In the first series, the amplitude (55 μm), preload (0.2 MPa), and main load (0.4 MPa) were maintained at constant values while the welding time was varied between 0.7 and 1.3 seconds in increments of 0.1 seconds. Using the results obtained from this series, we designed the second series of experiments, in which the main load and amplitude were modified at three levels each, as outlined in Table 1.

Table 1. The values of the welding parameters

Parameters		Levels		
		-1	0	1
x_1	Welding pressure in psi	45	50	55
x_2	Amplitude, μm	50	55	60

The quality of the seams formed during the welding tests was characterized by the load required to induce failure. The tests were conducted using an ELT-Schaltschrank tensile testing machine, with a displacement rate set at 10 mm/min.

3. Results

3.1. Effect of welding time

In the first series of experiments, we changed the welding time. The obtained results are illustrated graphically in Figure 2.

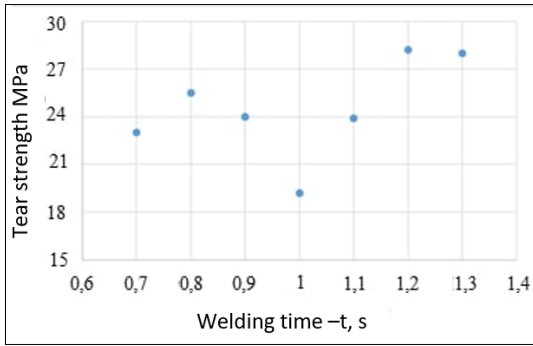


Fig. 2. Development of the strength of the seams as a function of time.

The figure clearly illustrates that welding time significantly influences the strength of the seam. During the experiments, 15 welds were performed at each test point, and the figure displays the average values. The lowest quality joint was obtained with a welding time of 1 second, yielding a strength of 18.5 MPa, while the highest strength of 28.2 MPa was measured at a welding time of 1.2 seconds.

Additionally, the figure demonstrates a fluctuation in welding quality associated with the characteristic of ultrasonic welding, which is also reflected in the variation of the hardness parameter as a function of distance [7].

3.2. Effect of main load and amplitude

Based on the results of the first series of experiments, we established that the highest weld strength was achieved at a welding time of 1.2 seconds, given the same welding parameters. Therefore, with this welding time held constant, we conducted the second series of experiments, incorporating the input variables presented in Table 1. A comprehensive experimental design was employed, allowing for the examination of all parameter combinations across nine measurement points.

The results are illustrated graphically in Figure 3.

The figure clearly demonstrates that the main load has a significantly smaller effect on seam strength compared to amplitude. However, when varying the amplitude, it is evident that the highest breaking force was achieved at an amplitude of 55 μm , while seam strength values for amplitudes below 50 μm were comparatively lower.

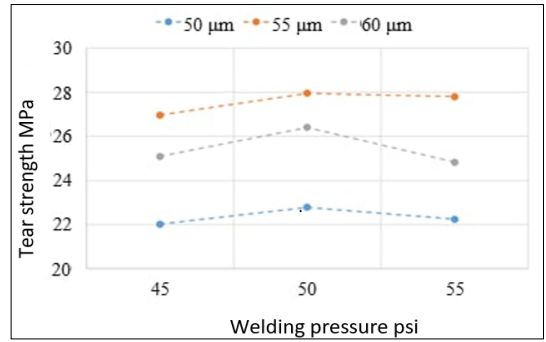


Fig. 3. The strength of the seams as a function of the amplitude and the main load.

4. Conclusions

Based on the experimental results, further investigations are necessary to draw definitive conclusions. The welding of polypropylene sheets in the industry is currently an extensively researched area, thus supporting the continuation of this study, with the findings aligning with existing literature. The conclusions derived from the measurements of the current research are as follows:

- The highest tear strength was obtained with a welding time of 1.2 seconds.
- Changing the amplitude had a greater influence on the holding capacity of the seams than changing the main load.
- The highest seam strength was measured at an amplitude of 55 μm .

References

- [1] Hamdi M., Saleh M. N., Poulis, J. A.: *Improving the adhesion strength of polymers: Effect of surface treatments*. Journal of Adhesion Science and Technology, 34/17. (2020) 1853–1870. <https://doi.org/10.1080/01694243.2020.1732750>
- [2] Cui C., Liu W.: *Recent advances in wet adhesives: Adhesion mechanism, design principle and applications*. Progress in Polymer Science, 116. (2021) 101388. <https://doi.org/10.1016/j.progpolymsci.2021.101388>
- [3] Acherjee B.: *Laser transmission welding of polymers – A review on process fundamentals, material attributes, weldability, and welding techniques*. Journal of Manufacturing Processes, 60. (2020) 227–246. <https://doi.org/10.1016/j.jmapro.2020.10.017>
- [4] Stadler R. G., Horváth R.: *Investigation of Welding Forces and Weld Strength for Friction Stir Welding of Acrylonitrile-Butadiene-Styrene (ABS) Plates*. Acta Materialia Transylvanica 6/1. (2023) 53–58. <https://doi.org/10.33924/amt-2023-01-09>

- [5] Kumar S., Wu C. S., Padhy G. K., Ding W.: *Application of ultrasonic vibrations in welding and metal processing: A status review*. Journal of Manufacturing Processes, 26. (2017) 295–322. <https://doi.org/10.1016/j.jmapro.2017.02.027>
- [6] Schramkó M., Nyikes Z., Pinke P., Tóth L., Kovács T. A.: *Experimental Study of a Vehicle Component Ultrasonic Welding Failure*. In: International Scientific Conference Fundamental and Applied Scientific Research in the Development of Agriculture in the Far East, January 2023. Cham, Springer Nature Switzerland, 2023. 548–554. https://doi.org/10.1007/978-3-031-36960-5_62
- [7] Schramkó M., Nyikes Z., Jaber H., Kovács T. A.: *Dissimilar Joining by Ultrasonic Welding*. Journal of Hunan University Natural Sciences, 49/3. (2022). <https://doi.org/10.55463/issn.1674-2974.49.3.20>
- [8] Temesi T., Czigany T.: *Integrated Structures from Dissimilar Materials: The Future Belongs to Aluminum–Polymer Joints*. Advanced Engineering Materials, 22/8. (2020) 2000007. <https://doi.org/10.1002/adem.202000007>
- [9] Kiss Z., Temesi T., Bitay E., Bárány T., Czigány T.: *Ultrasonic welding of all-polypropylene composites*. Journal of Applied Polymer Science, 137/24. (2020) 48799. <https://doi.org/10.1002/app.48799>
- [10] Kawasaki S., Naito K., Ishida O., Shirai T., Uzawa K.: *Infrared-thermography measurement of temperature distribution in carbon fiber–reinforced polypropylene during ultrasonic welding*. Composites Part A: Applied Science and Manufacturing, 177. (2024) 107887. <https://doi.org/10.1016/j.compositesa.2023.107887>
- [11] Raza S. F., Khan S. A., Mughal M. P.: *Optimizing the weld factors affecting ultrasonic welding of thermoplastics*. The International Journal of Advanced Manufacturing Technology, 103/5. (2019). 2053–2067. <https://doi.org/10.1007/s00170-019-03681-7>
- [12] Rajput C., Kumari S., Prajapati V., Abhishek K.: *Experimental investigation on peel strength during ultrasonic welding of polypropylene H110MA*. Materials Today: Proceedings, 26. (2020). 1302–1305. <https://doi.org/10.1016/j.matpr.2020.02.259>
- [13] Bárány T., Karger-Kocsis J. (eds.): *Polypropylene Handbook: Morphology, Blends and Composites*. Springer International Publishing, 2019. <https://doi.org/10.1007/978-3-030-12903-3>

Effects of Femtosecond Laser Surface Treatment on Glass Fiber Reinforced Composites Produced by Pultrusion

Dániel VACZKÓ,¹ Zoltán WELTSCH,² Róbert KERESZTES³

¹ Department of Innovative Vehicles and Materials, John von Neumann University, Kecskemét, Hungary, vaczko.daniel@nje.hu

² Department of Road and Rail Vehicles, Zalaegerszeg Innovation Park, Széchenyi István University, Győr, Hungary, weltsch.zoltan@sze.hu

³ Mechanical Engineering Technology Institute, Faculty of Mechanical Engineering, Szent István University, Gödöllő, keresztes.robert.zsolt@uni-mate.hu

Abstract

In this study, we evaluated the effectiveness of laser surface treatment on flat, glass fiber-reinforced profiles produced by pultrusion. The experiments used a Coherent Monaco 1035-80-60 femtosecond laser, where the main parameter was laser power. The treated samples were examined with an Olympus OLS5000 confocal microscope, measuring the depth and area of the grooves created by the laser beam. The data were plotted as a function of power. Our results show that the increase in depth is not proportional to power, while there is a close correlation between changes in depth and area. These findings shed new light on the potential industrial applications of laser surface treatment for pultrusion-manufactured glass fiber-reinforced profiles, particularly concerning surfaces prepared for bonding.

Keywords: laser surface treatment, femtosecond laser, pultrusion, bonding technology, glass fiber.

1. Introduction

Pultrusion is a continuous manufacturing process specifically used for the production of glass fiber reinforced plastics. In this process, reinforcing fibers, such as glass fibers, are first drawn through a resin bath and then pulled through a long, heated die where the resin polymerizes, creating long and rigid composite elements with the desired profile. Pultrusion enables the rapid and cost-effective production of high-strength and corrosion-resistant composite structural elements [1]. The process is illustrated in Figure 1.

The extensive use of glass fiber reinforced plastics in the industry, especially in vehicle manufacturing and construction, is advantageous due to their high strength and corrosion resistance. However, the weak surface energy of glass fiber reinforced plastics limits their adhesive properties, presenting challenges for bonding technologies, particularly in the areas of adhesion and lamination [2].

The femtosecond laser uses short laser pulses, allowing for the modification of surface microstructures without thermally damaging the substrate. This surface treatment method is particularly beneficial for preparing plastic surfaces, as it improves surface tension and thereby the quality of bonds [3].

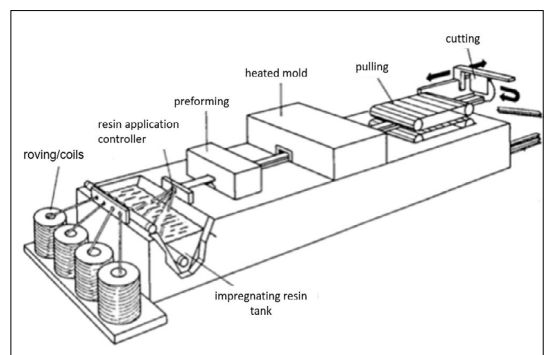


Fig. 1. The pultrusion process. [5]

Research by Banks and colleagues demonstrates that femtosecond lasers can be used to create complex, high-precision cuts and holes in various materials without causing damage to the surrounding material. During such operations, the laser pulses can be directed with such precision that the structural integrity of the remaining material remains completely intact, which is critical for certain industrial applications [4].

The aim of this study is to investigate the effects of surface treatments conducted with the Coherent Monaco 1035-80-60 femtosecond laser on pultrusion-manufactured profiles, particularly in terms of improving bonding properties such as bond strength and surface energy. The results highlight the potential industrial applications of femtosecond lasers in the surface treatment of composite materials.

2. Experiments

2.1. Surface Treatment and Sample Preparation

In the research, we used flat glass fiber-reinforced plastic profiles produced by pultrusion, with the following composition: glass content 64%, Barcol hardness 48, aluminum trihydrate (ATH) 21.8 %, and the base resin ISO NPG. The preparation of the samples included cutting to size and cleaning the surfaces with methanol before treatment to remove any surface contaminants. The surface treatment was conducted using a Coherent Monaco 1035-80-60 femtosecond laser (Figure 2), with power as the variable. The other parameters were: pulse duration 277 fs, pulse frequency 750 kHz, and feed rate 1 m/s. The laser power was adjusted in 10 % increments from 10 % to 100 %. By varying the power, we

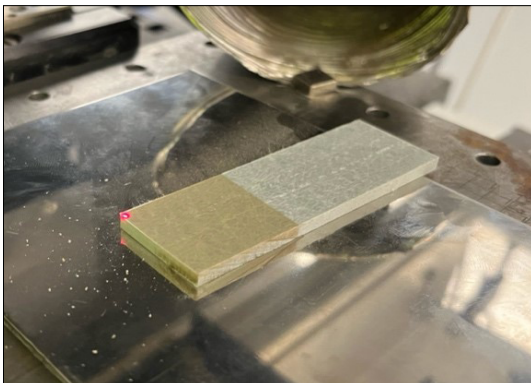


Fig. 2. Surface Treatment with Femtosecond Laser.

produced different samples, which were later examined with a confocal microscope.

2.2. Microscopic Analysis

To examine the effects of the laser treatment, the surface structure of the samples was analyzed using an Olympus OLS5000 confocal microscope, with a 20× objective for more detailed investigation of the surface structure (Figure 3). The microscopic examinations were conducted in a climate-controlled room to ensure minimal environmental impact on the samples and the accuracy of the measurements.

Data collection and analysis were conducted using the microscope's proprietary software, which allowed for accurate and reliable evaluation of the measured data. During the measurements, the depth and area of the grooves created by the laser beam were measured. The software is capable of creating 3D topographies (Figure 4). The image may include minimal noise, which appears as spikes; these were reduced with noise filtering.

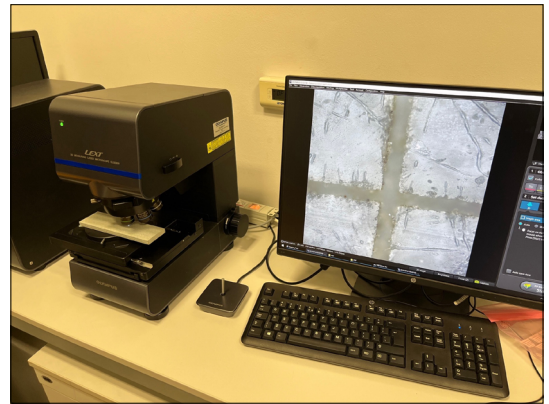


Fig. 3. Olympus OLS5000 Microscope.

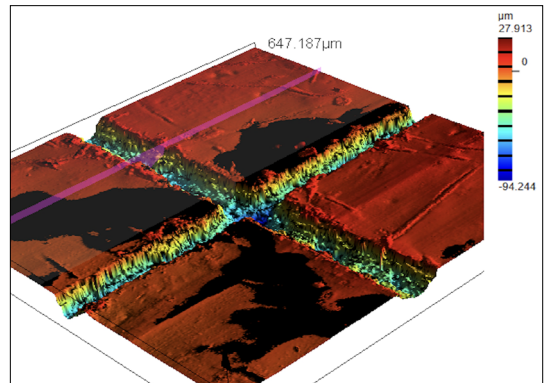


Fig. 4. 3D Topography, with Depths Indicated by Colors.

For depth and area measurements, a cross-sectional image of the groove was necessary, and the average dimensions of a 300 μm section of the groove were considered.

3. Results

During the investigation, the microscopic analysis of plastic profiles treated with the Coherent Monaco 1035-80-60 femtosecond laser provided important information on the impact of laser power on surface structure.

The graph shows that both the depth and area increase significantly with the rise in laser power. At the 10 % power level, the groove depth was approximately 10 μm , while the area was around 1000 μm^2 . As the power increased to 100 %, the groove depth approached 60 μm , and the area exceeded 2500 μm^2 .

In the 0–20 % range, the laser power is too low to create significant changes, so the depth and area remain low. In the 20–40 % range, as the power increases, the depth and area grow rapidly since the laser provides enough energy to modify the surface structures. In the 40–50 % range, the growth rate slows down, indicating that the laser power is nearing its maximum efficiency. However, in the 80–100% range, the growth slows down again, and a slight decrease can be observed, likely due to partial melting of the resin, which flows back into the microgrooves, reducing their depth and area.

Based on the obtained data, we created a graph that illustrates the changes in groove depth and area as a function of laser power. This graph clearly shows the relationship between the increase in power and the size of the groove (Figure 5).

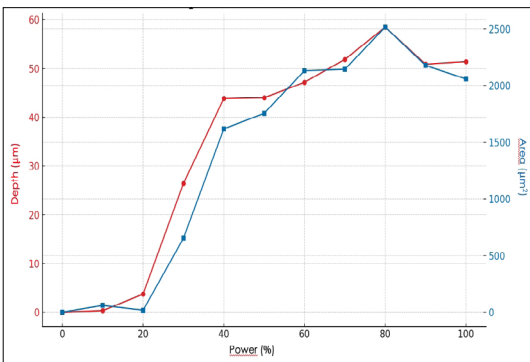


Fig. 5. Variation of Depth and Area as a Function of Power.

4. Conclusions

The microscopic analyses conducted during the research and the thorough evaluation of the obtained data allowed us to gain a comprehensive understanding of the effects of using a femtosecond laser for surface treatment of pultruded, glass fiber-reinforced plastic (GFRP) profiles. The results clearly demonstrated that increasing the laser power proportionally increases the depth and area of microgrooves on the GFRP surfaces, which significantly influences the surface morphology.

Based on the analysis of the graph, the changes in depth and area with increasing power do not follow a simple linear or exponential trend but show different patterns at various stages. In the low-power range, the increase is minimal; at medium power, rapid growth is observed, while in the high-power range, the growth slows down and sometimes even decreases. This correlation supports the applicability of laser treatment for targeted modification of plastic surface properties.

Microscopic examinations revealed that surface treatment with higher power results in a more uniform microstructure, which could be more favorable for adhesive processes. A uniform microstructure can enhance adhesion, facilitating better bond strength.

Due to the melt occurring at high power levels, it will be worthwhile to investigate how the base material responds to multiple treatments under optimal settings in the future.

The study's results may contribute to the advancement of industrial plastic processing, particularly in areas where surface properties such as adhesiveness and mechanical durability are crucial.

Acknowledgements

The research presented in the article was created with the support of the grant numbered 2020-1.1.2-PI-ACI-KFI-2020-00052. The project was implemented within the framework of the call announced by the Ministry of Innovation and Technology and the National Research, Development and Innovation Office.

References

- [1] Fairuz A. M. et al.: *Polymer composite manufacturing using a pultrusion process: A review*. American Journal of Applied Sciences, 11/10. (2014) 1798–1810. <https://doi.org/10.3844/ajassp.2014.1798.1810>.
- [2] Gattass R. R., Mazur E.: *Femtosecond laser micro-*

machining in transparent materials. Nature photonics, 2/4. (2008) 219–225.

<https://doi.org/10.1038/nphoton.2008.47>

- [3] Sugioka K. et al.: *Femtosecond laser 3D micro-machining: a powerful tool for the fabrication of microfluidic, optofluidic, and electrofluidic devices based on glass*. Lab on a Chip, 14/18. (2014) 3447–3458.
- [4] Banks Paul Stuart et al.: *Femtosecond laser materials processing*. Commercial and Biomedical Applications of Ultrafast Lasers II. Vol. 3934. SPIE, 2000.
- [5] Czvikovszky T., Nagy P., Gaál J.: *A polimertechnika alapjai*. Műegyetemi kiadó, Budapest, 2000.

<https://doi.org/10.1039/C4LC00548A>

<https://doi.org/10.1117/12.386356>